Materials Advances

ROYAL SOCIETY OF CHEMISTRY

REVIEW

View Article Online
View Journal | View Issue

Cite this: *Mater. Adv.*, 2023, 4, 1226

Heteroatom-doped transition metal hydroxides in energy storage and conversion: a review

Yaqi Qin,†[a] Guoping Lu, †*[a] Feng Yang,[a] Chunhua Xu,[a] Shuaijie Jiang,[a] Yuqiu Wang,[a] Yuxin Tang*[b] and Pengcheng Wang *[a]

Received 27th October 2022,
Accepted 11th January 2023

DOI: 10.1039/d2ma01002j

rsc.li/materials-advances

High performance transition metal hydroxides (TMHs) are promising energy storage materials due to their simple and low-cost preparation process, high surface area, easy tunable composition, and so on. Heteroatom doping is an extensive approach adopted to tailor, both physically and chemically, the properties of TMHs, such as their lattice structure, electronic structure, lattice defects and diffusion behavior, so as to alter their catalytic performance for various redox reactions. Heteroatom doping can also improve the overall performance of TMH electrode materials in terms of specific capacitance and charge–discharge rate. Recently, the applications of heteroatom doping engineering in developing various TMHs/TMH-based composite materials with specific structures or functions in the fields of energy conversion and storage have been extensively explored. To this end, we review the latest developments in the heteroatom doping of TMHs in the fields of energy conversion and storage *via* metal doping, non-metal doping, and co-doping engineering. Then, the principles and effects of heteroatom doping in TMHs are discussed and generalized. Finally, the challenges and opportunities of heteroatom doping in TMHs are disclosed to provide insights regarding the further development of this research.

1. Introduction

With the energy shortage and increasingly serious energy-related pollution, various energy storage devices and clean energy sources (including metal batteries and supercapacitors (SCs), H_2O splitting, fuel cells and CO_2 conversion) have received extensive attention from researchers.[1–3] As representatives of modern energy storage equipment, SCs and battery devices have been extensively used in daily life to supply power for various portable electronic devices.[4,5] As a clean energy source, H_2 with high efficiency and low emission is the best alternative to fossil fuels. H_2O splitting to generate H_2 and O_2 is one of the most economical and environmentally friendly methods.[6] Meanwhile, when the urea oxidation reaction (UOR) is used as the anode reaction for water splitting to generate H_2, its theoretical voltage (0.37 V *vs.* RHE) is much

[a] *School of Chemistry and Chemical Engineering, Nanjing University of Science and Technology, Nanjing 210094, China. E-mail: glu@njust.edu.cn, alexwpch@njust.edu.cn*
[b] *Institute of Applied Physics and Materials Engineering, University of Macau, Macau, P. R. China. E-mail: yxtang@um.edu.mo*
† These authors contributed equally to this paper.

Yaqi Qin

Yaqi Qin is currently a doctoral candidate at Nanjing University of Science and Technology, and she is engaged in the design, synthesis and application research of electrocatalytic materials under the guidance of Professor Pengcheng Wang. At present, she has published an article on the design and synthesis of supercapacitor electrodes.

Guoping Lu

Guo-Ping Lu received his PhD degree in Chemical Engineering and Technology from Nanjing University of Science & Technology in 2013. He is currently an associate professor in the School of Chemistry and Chemical Engineering at Nanjing University of Science & Technology. His research interests focus on heterogeneous catalysis for green organic synthesis and biomass conversion.

lower than the traditional H_2O electrolysis voltage (1.23 V *vs.* RHE), which can produce H_2 with lower energy consumption, providing a prospect for the purification of urea-rich wastewater.[7] The electrocatalytic reduction of CO_2 reaction (CO_2RR) to produce a liquid fuel can not only alleviate the energy crisis but also solve the environmental problems caused by the greenhouse effect.[8]

However, numerous obstacles remain in the development of energy storage devices. Normally, conventional Li batteries have relatively low ionic resistance, leading to some drawbacks such as safety issues and insufficient lifetime.[2] The disadvantage of SCs regarding low energy density (SCs: 1–10 W h kg^{-1} *vs.* batteries: 10–100 W h kg^{-1}) has also been identified as a major challenge for their development.[9] The anodic oxygen evolution reaction (OER) of H_2O splitting requires a high overpotential, which increases energy consumption.[7] In essence, the performance of energy storage devices is limited by the inherent properties of active materials. Therefore, various electrode materials and electrocatalysts with specific structures or functionalities are rationally designed to improve the development of energy devices.[10–12]

Traditional transition metal hydroxides (TMHs) as a promising class of electrode materials are mainly composed of transition metal cations (such as Co^{2+}, Ni^{2+}, Mn^{2+}, and Cr^{3+}) and OH^-.[9,13–15] They have been employed in various improved energy devices owing to their simple synthetic process, cheapness, unique structure and properties.[16,17] TMHs can provide high capacitance from reversible faradaic reactions between electrode materials and electrolyte ions, and can store much more energy for SCs than carbon-based materials and achieve better electrochemical stability than polymer materials.[9] The unique e_g orbital occupancy of transition-metal OER electrocatalysts makes them highly active to absorb OER intermediates to strengthen electrocatalytic activities.[18,19] Unfortunately, the low inherent conductivity of TMHs limits their diffusion rate of electrons, and their structures easily collapse in an alkaline medium. These issues have seriously hindered their applications in energy storage and conversion. Therefore, numerous studies about the structure optimization of TMHs have been reported to overcome these issues.[15] There are four main strategies for their modification (Fig. 1) including morphology and nanostructure engineering,[20] defect manufacturing,[21] conductive substrate introducing,[18] and heteroatom doping.[22] The construction of 2D nano-sheets/wires using TMHs could increase their specific surface area.[23,24] The combination of TMHs with conductive matrixes/carriers (such as conductive polymers and carbon-based materials) may avoid structural accumulation, reducing the "dead surface" generated in the process of conventional preparation electrodes.[20,25] Creating defects can produce more active sites, which more easily exposes TMH matrix to reduce the contact resistance.[26] However, these modification strategies are essential to increase the contact area between the electrode and the electrolyte and promote the charge transmission capacity of

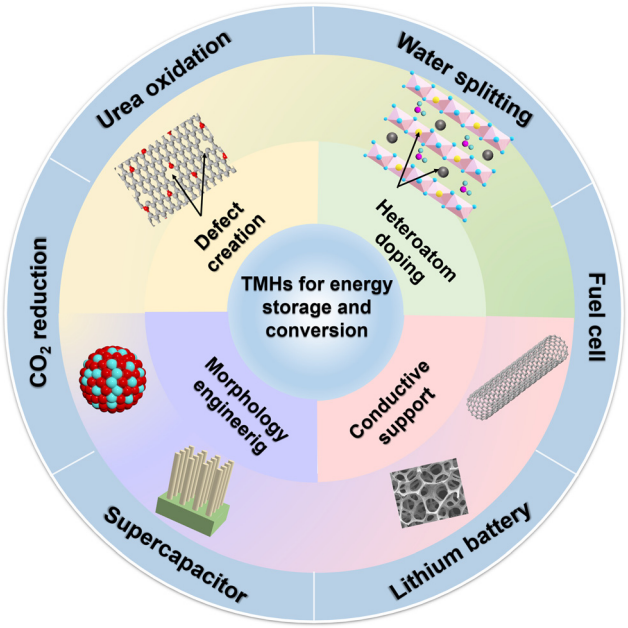

Fig. 1 The modification and related energy applications of TMHs.

Yuxin Tang

Yuxin Tang is a professor in the College of Chemical Engineering at Fuzhou University. He obtained his BS and MS degrees at the Nanjing University of Aeronautics and Astronautics in 2006 and 2009, respectively, and graduated from Nanyang Technological University with a PhD in materials Science (2013). His research interests include solid-state and fast charging energy storage devices and the development of real-time electrochemical reaction monitoring techniques.

Pengcheng Wang

Pengcheng Wang obtained his BSc in 2008 and PhD in 2013 at Nanjing University of Science and Technology (NJUST) and was a postdoc at the National Institute of Advanced Industrial Science and Technology (AIST) from 2013 to 2014. He joined NJUST in 2014 and became a professor in 2020. His research interest includes energetic materials, energy storage materials and electrochemical reaction.

TMHs. In addition, doping heteroatoms can regulate the electronic structures of metal ions or produce new active metal sites in TMHs.[27] It has been proved that the doping of active hetero-metal ions into singly active metal hydroxide structures may help widen their interlayer space and reduce their mechanical stress during the charge/discharge process, thereby leading to an obvious increase in their capacitive performance.[28]

Compared with other approaches, doping engineering is a simple and efficient method to improve the composition and performance of TMHs. Doping engineering can be divided into metal doping and non-metal doping based on the type of doped ions.[29,30] Metal doping involves the introduction of objective metal cations outside the main body. Since there are electronic interactions among multiple metals/elements, the performance of multi-metal TMHs is superior to that of single-metal TMHs. Non-metal doping involves the introduction of non-metal anions with high solubility constants to completely or partially replace the existing anions of TMHs or doping them into the host lattice of the TMHs.[28,31] The synergic effects of doped metal ions may influence the electronic structure of TMHs, improving their inherent electrochemical performance, activity, and conductivity. Co-doping involves selecting two or more dopants and combining a variety of doping principles to enhance the advantages of heteroatom doping.[32] At the same time, the choice of various dopants not only considers the doping principle but also considers the mutual balance among the plurality of dopants, thereby producing a positive effect.

Generally, there are four functions of heteroatom doping on TMHs (Fig. 2): (1) heteroatom doping can form multi-component TMHs to adjust the metal valence ratio; (2) it could regulate and increase active metal sites; (3) the doped heteroatoms could tune electronic states, thereby improving the inherent conductivity of these materials; and (4) it could increase the interlayer spacing to expand the ion transport pathway, decreasing contact resistance between transition metal elements and OH^-.[33] More critically, heteroatom doping provides numerous crucial possibilities and application prospects in the development of multi-element TMHs owing to the wide variety and compatibility of heteroatoms.[34,35]

So far, the applications of heteroatom-doped TMHs in energy storage and conversion devices are increasing, but few attempts systematically summarize their applications in this field. In order to witness the important development of heteroatom-doped TMHs in the energy field, we provide this in-time review by classifying heteroatom-doped TMH technologies into metal doping, non-metal doping and co-doping according to the compositional characteristics of TMHs. The applications of heteroatom-doped TMHs in H_2O splitting, fuel cell and lithium battery catalysis as well as supercapacitor energy storage are also summarized. Furthermore, the principles and effects of doping are also introduced in detail. Finally, we summarize both challenges and opportunities of heteroatom doping in TMHs to demonstrate the future development direction of the heteroatom doped TMH strategy, aiming to stimulate more new and efficient investigations in this field.

2. Doping principles and effects

It is well known that the electrochemical properties of TMH materials depend primarily on certain structural characteristics: (1) the specific surface of TMHs can be controlled, such as constructing core–shell, linear, cluster, granular and nanostructures, which is beneficial to increase the capacitance and reduce the contact resistance of capacitors. (2) Modification of TMHs at the molecular level can increase the synergistic effects between the active sites and the components, thereby improving the catalytic reaction kinetics and accelerating the HER/OER catalytic process. (3) The regulation of the electronic environment affects the interfacial charge transfer and inherent

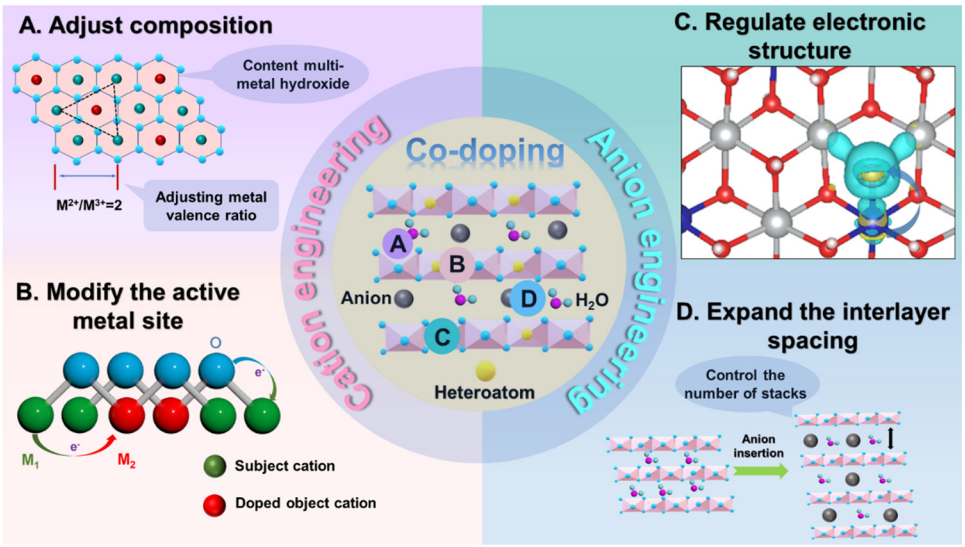

Fig. 2 The functions of heteroatom-doping on TMHs.

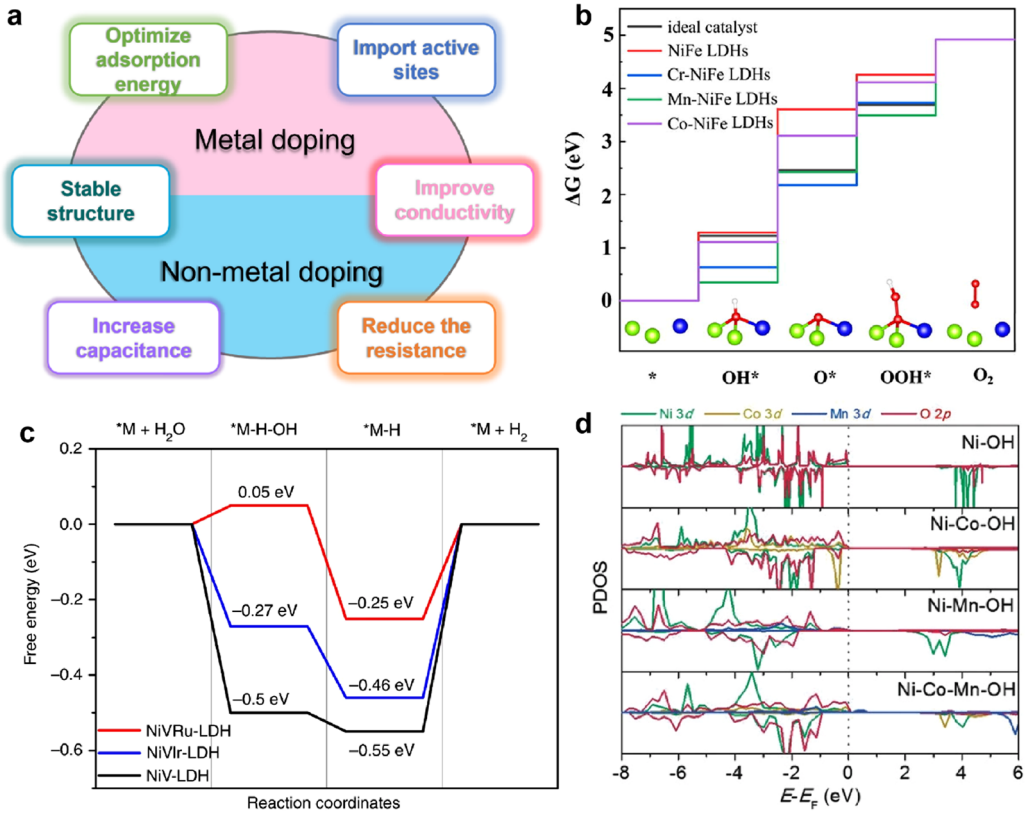

Fig. 3 (a) Schematic diagram of the advantages of doping-modified TMHs. (b) The free energy diagram of the OER on un-doped and doped NiFe LDHs. Reproduced with permission from ref. 38 © 2020 Elsevier Inc. (c) The free energy diagram of the HER on the NiV-LDH, NiVRuLDH, and NiVIr-LDH catalysts. Reproduced with permission from ref. 39 © 2019 nature. (d) Partial density of state diagrams for Ni, Ni–Co, Ni–Mn, and Ni–Co–Mn hydroxide systems. Reproduced with permission from ref. 40 © 2017 WILEY-VCH Verlag GmbH & Co. KGaA, Weinheim.

conductivity and improves the internal electrocatalytic activity of TMHs.

Therefore, heteroatom doping engineering enabling the structure of TMHs will be effectively modified, thereby producing an intrinsic change in their electrochemical properties. Here, we summarized the doping principles of various element types and the correlation between doped elements and the electrochemical properties of TMHs. Specifically, in order to better discuss the principle and function of doping, we divide the doped elements into the following categories: metal doping and non-metal doping (Fig. 3(a)).

2.1. Metal doping

Generally, metal doping can significantly improve the electrochemical properties of TMHs. First, inactive metal ion (such as Mn^{2+} and Al^{3+}) doping can cause the orbital hybridization of relatively low valence metal ions, which may stabilize the layer structure of the TMHs to effectively increase the capacity.

Second, doping of active metal ions such as Ni^{2+}, Co^{2+}, Fe^{2+}/Fe^{3+}, and Zn^{2+} can introduce new active sites in TMHs, which may accelerate charge transfer and electron conductivity to enhance the electrocatalytic properties of the HER and the OER.

Finally, Cr^{6+}, Ta^{5+} and V^{5+} having high valence metal ion doping may introduce changes in the electronic structure and overcome the H_2O adsorption in the oxidation process.

2.2. Non-metal doping

From the perspective of non-metal doping modified TMHs, the doping of elements (S, P and N) may regulate material morphology and produce more defects, edge sites, and more empty d orbitals. These may contribute to exposing TMH based materials to reduce the contact resistance.

In addition, high electronegativity atom doping, F and Cl, may form stable M–F bonds in TMHs, resulting in changes in the charge density and the production of active centers to increase conductivity and stability.

Furthermore, when the inorganic (NO_3^-, CO_3^{2-}, SO_4^{2-}, PO_4^{3-}) or organic anions (AcO^-, $C_{17}H_{35}COO^-$) with a large radius are embedded in the LDH layer, the layer spaces may be expanded, and the micro-variation of the lattice is changed. Accordingly, these may cause expansion and lattice strain of the intermediate layer in the LDHs to attenuate the resistance of the interaction between the TMHS active component and OH^- and increase the transmission capacity of ions.

2.3. Density functional theory

A recent discovery using density functional theory (DFT) calculations and theoretical computational models provides new guidelines for designing innovative catalyst materials and the electronic structure of the catalyst. In addition, the scaling

relationship between the properties of catalytic materials and reaction intermediates can expand our understanding of the reaction mechanism at the molecular level.[36] Therefore, DFT calculations provide a simple and efficient method to establish the relationship between the structure and performance of heteroatom-doped TMHs.

The HER and OER are two and a half reactions in the electrocatalysis process, and high-efficiency electrocatalysts are needed to reduce the overpotential caused by the slow transfer of multiple proton-coupled electrons in these two reactions.[37] The proposed OER process under alkaline conditions consists of four elementary stages: M*, M–OH, M–O, and M–OOH. Gao *et al.*[38] designed a series of transition metal (Cr, Mn and Co) doped NiFe-LDHs to study the doping effect in the OER. The energy profiles of the OER on the un-doped and doped NiFe-LDHs are shown in Fig. 3(b), the largest energy uphill of each catalyst is the potential-determining step. When NiFe-LDHs doped with other transition metals, the Gibbs free energies of O*, OH* and OOH* intermediates calculated by DFT decrease significantly, indicating that the guest metal atoms play a role in active NiFe LDH, resulting in stronger binding of intermediates.

Yang *et al.*[39] reported a method of site-selective incorporation of a noble metal (Ru or Ir) into NiV-LDH to investigate the original relationship between the activity of the HER and the doping effect at atomic levels. In Fig. 3(c), Ru and Ir doping can accelerate both Volmer and Heyrovsky steps in alkaline media, and Ru is more conducive to the HER. This demonstrates that doping of noble metals can reduce the energy barrier in the Volmer and Heyrovsky steps of the HER.

In order to rationally design nickel hydroxide-based electrode materials for fast energy storage, it is necessary to fully understand the structural evolution, charge storage mechanism and the contribution of the redox reaction to the capacity of the electrode. Liu *et al.*[40] deeply explored the reasons why cation doping can improve the performance of $Ni(OH)_2$ electrode materials in supercapacitors. The electrochemical performance of nickel hydroxides potentially depends on their deprotonation energies, which are calculated by DFT using a structural slab. The calculated Gibbs free energy change after deprotonation determines the driving force for the charge–discharge process and potentially affects the electrochemical properties. Depending on the partial density of state (PDOS) diagrams in Fig. 3(d), it is found that Co or Mn substituted in $Ni(OH)_2$ diminish band gaps by filling the very top of the valence band near the Fermi level, which reveals that cation doping can improve the electronic conduction and excitation of electrode materials. The difficulty of charge transfer between metal cations and O in the absence of Mn in hydroxide could result in poor conductivity and sluggish charge–discharge kinetics.

DFT allows us to examine the essential influence of heteroatom doping on TMHs, check all hypotheses, and select suitable candidate heteroatoms to combine them with existing TMHs, to adjust the details of the atomic scale. DFT calculations have been successfully applied to analyze activation barriers, adsorption energies and reaction thermodynamics, which can quantify the deprotonation energy, and provide a basis for the design and prediction of heteroatom-doped TMH electrode materials for fast energy storage.

3. Metal engineering

3.1. Single-metal TMHs (LSHs)

Single metal hydroxides (LSHs) are generally divided into two categories: $M(OH)_2$ and $M(OH)_{(2-x)}A_x^{m-}\cdot nH_2O$. $M(OH)_2$ is the original brucite phase (*e.g.*, β-$Ni(OH)_2$ and β-$Co(OH)_2$),[41] wherein the divalent metal cations in the octahedral structure are coordinated to six OH^- ions and share edges, with no ion insertion in the neutral layer.[42] $M(OH)_{(2-mx)}A_x^{m-}\cdot nH_2O$ is a hydrotalcite phase (such as α-$Ni(OH)_2$ and α-$Co(OH)_2$), where A^{m-} represents an intercalated anion, replacing OH^- in the interlayer channel.[43]

Recently, LSHs with various morphological characteristics have been applied as electrode materials in various energy storage devices. However, α-$M(OH)_2$ exhibits poor cycling stability and is easy to convert β-$M(OH)_2$ and lost crystal H_2O in alkaline electrolytes, resulting in structural degradation. Therefore, incorporation of metals with different valence states (such as Mn^{2+}, Zn^{2+} and Al^{3+} Fe^{2+}/Fe^{3+}) into LSHs is a general strategy to enhance their intrinsic electrocatalytic activities and structural stability.[34,44]

3.1.1. Mn-doped LSHs. It has been reported that low doping of manganese can reduce the band gap and generate impurity states to increase the conductivity. Chen *et al.*[45] prepared an Mn doped $Co(OH)_2$ electrode material for supercapacitors. Mn doping increases the rate of electron transport and stability of $Co(OH)_2$ owing to the unique 2D structure of Mn doped $Co(OH)_2$. Compared with the original $Co(OH)_2$, the Mn-doped nanoplate electrode shows a high specific capacitance of 1915.88 F g^{-1} at 1.0 A g^{-1}. At a current density of 10.0 A g^{-1}, it still exhibits a capacity retention rate of 93.5% after 5000 charge–discharge cycles (Table 1, entry 1).

Yin *et al.*[46] proposed a novel strategy to improve the stability of the $Ni(OH)_2$ electrode and modulate the electronic configuration and the layer stacking mode of α-$Ni(OH)_2$ through controlling the Mn doping level and the occupied site (Fig. 4(a)–(c)). Due to the presence of Mn^{4+} ions, more anions are accommodated in the interlayers to increase the spacing along the *c* direction. Finally, the optimal NiMn-LDH has a high capacity (1498 C g^{-1} at 2 A g^{-1}), great rate performance and excellent cycle performance (almost 100% capacity retention after 30 000 cycles at 50 A g^{-1}) (Table 1, entry 2).

3.1.2. Zn-doped LSHs. $Ni(OH)_2$ has been widely studied for its low cost and theoretical capacity up to 2082 F g^{-1}, which makes $Ni(OH)_2$ an ideal electrode material for HSCs. However, there are various issues with $Ni(OH)_2$ based electrodes such as poor electrical conductivity and rate capability. Zn has received much attention due to its low-cost, wide availability and large concentration of holes if replacing the other metal ions. Moreover, adding a proper amount of Zn element can accelerate the electron transfer and improve the electrochemical activity and

Table 1 Summary of capacitor electrode performance

Entry	The doped heteroatom	Electrodes	Specific capacitance ($F\ g^{-1}$)	Rate performance	Cycle performance ($5\ A\ g^{-1}$)	Highest energy density: ($W\ h\ kg^{-1}$)	Highest power density: ($W\ kg^{-1}$)	Electrolyte	Ref.
1	Mn	Mn doped $Co(OH)_2$	1915.88 ($1\ A\ g^{-1}$)	63.18% ($20\ A\ g^{-1}$)	93.5% (5000) at $10\ A\ g^{-1}$	—	—	2 M KOH	45
2	Mn	NiMn-LDH	1498 C g^{-1} ($2\ A\ g^{-1}$)	61.08% ($50\ A\ g^{-1}$)	96.5% (10 000) at $10\ A\ g^{-1}$	62.7	375.2	6 M KOH	46
3	Zn	Zn doped $Ni(OH)_2$@CNTs	750.5 C g^{-1} ($0.5\ A\ g^{-1}$)	72.9% ($10\ A\ g^{-1}$)	115.8% (5000) at $6\ A\ g^{-1}$	51.3	409.6	2 M KOH	46
4	Zn	NiZn−OH/rGO	615.4 C g^{-1} ($1\ A\ g^{-1}$)	62.3% ($30\ A\ g^{-1}$)	89.7% (10 000)	53.7	825.1	—	48
5	Al	Al-doped $Ni(OH)_2$	2606 ($1\ A\ g^{-1}$)	44.5% ($20\ A\ g^{-1}$)	46.5% (1200) at $10\ A\ g^{-1}$	—	—	6 M KOH	50
6	Al	Al^{3+}-doped α-$Ni(OH)_2$	1750 ($1\ A\ g^{-1}$)	92% ($10\ A\ g^{-1}$)	72% (2000) at $16\ A\ g^{-1}$	49.6	573.8	6 M KOH	51
7	Zn	NiCoZn–LDH	1742 ($1\ A\ g^{-1}$)	77% ($10\ A\ g^{-1}$)	89% (40 000) at $10\ A\ g^{-1}$	37.2	362	3 M KOH	69
8	S	NiV-S	2270.4 ($2\ A\ g^{-1}$)	51.3% ($20\ A\ g^{-1}$)	91.9% (10 000) at $25\ A\ g^{-1}$	51	1600	1 M KOH	84
9	S	NiCo-LDH-S7.5	2417.7 ($1\ A\ g^{-1}$)	81.8% ($20\ A\ g^{-1}$)	90.19% (5000) at $2\ A\ g^{-1}$	73.57	375	2 M KOH	85
10	S	S-doped $Ni_2(OH)_2CO_3$ @MWCNTs	1158 ($1\ A\ g^{-1}$)	83% ($5\ A\ g^{-1}$)	98% (20 000)	45	400	6 M KOH	87
11	F	F-doped α-$Ni(OH)_2$	1503 ($1\ A\ g^{-1}$)	48.7% ($20\ A\ g^{-1}$)	82% (9000)	67.4	400	2 M KOH	101
12	Cl	$Co(CO_3)_{0.35}$-$Cl_{0.20}(OH)_{1.10}$	9893.75 ($0.5\ A\ g^{-1}$)	—	75% (10 000) at $0.5\ A\ g^{-1}$	41.66	19.5	1 M KOH	104
13	N	$Ni(OH)_2$–N	434.7 mA h g^{-1} ($5\ A\ g^{-1}$)	91.7% ($20\ A\ g^{-1}$)	51% (1000) at $50\ A\ g^{-1}$	—	—	1 M KOH	107
14	Cl^-	α-$Ni(OH)_2$-DS NBHMs	1494 ($1\ A\ g^{-1}$)	30.3% ($8\ A\ g^{-1}$)	90.9% (500) at $4\ A\ g^{-1}$	—	—	1 M KOH	108
15	SO_4^{2-}	CoMn-LDH-SO_4	582.07 mC cm^{-2} ($2\ mA\ cm^{-2}$)	66.2% ($50\ mA\ cm^{-2}$)	89% (18 000) at ($10\ mA\ cm^{-2}$)	0.096 mW h cm^{-2}	1.5 mW cm^{-2}	1 M KOH	109
16	NO_3^-	Co–Al-LDH–NO_3^-	2230 ($1\ A\ g^{-1}$)	60% ($20\ A\ g^{-1}$)	—	—	—	1 M KOH	110
17	BO_2^-	PMNC g^{-1}-2	1890 ($0.5\ A{\cdot}g^{-1}$)	84% ($40\ A\ g^{-1}$)	83% (10 000)	41	216	6 M KOH	111
18	SDS	NiMn LDH-2	325 mA h g^{-1} ($1\ A\ g^{-1}$)	64.3% ($20\ A\ g^{-1}$)	89.65% (2000) at $20\ A\ g^{-1}$	46.5	688.3	1 M KOH	112
19	OA	NA-LDH-OA	1.040 C cm^{-2} ($1.68\ mA\ cm^{-2}$)	—	94.5% (2000) at $44.1\ mA\ cm^{-2}$	40.26	943	6 M KOH	113
20	$[CoOx_2]^{2-}$	I-$Co(OH)_2$ NSs	880 mA h g^{-1} ($1\ A\ g^{-1}$)	64.3% ($5\ A\ g^{-1}$)	99% (250) at $1\ A\ g^{-1}$	—	—	1 M $LiPF_6$	114
21	Cu/Ni	Cu-$Ni(OH)_2$	1832.5 mA h g^{-1} ($0.2\ A\ g^{-1}$)	—	72.5% (800) at $1\ A\ g^{-1}$	—	—	—	117
22	Al/Co	Al–Co co-doped α-$Ni(OH)_2$/GNS	2257 ($2\ mV\ s^{-1}$)	77.5% ($50\ mV\ s^{-1}$)	77% (1000)	—	—	6 M KOH	118
23	S/P	NiCo LDH-SP	3384.8 ($3\ A\ g^{-1}$)	66% ($20\ A\ g^{-1}$)	81.3% (5000) at $8\ A\ g^{-1}$	74.5	800	6 M KOH	120
24	C/N	C/N–$Ni(OH)_2$/Ni_xS_y	1731.2 ($0.5\ A\ g^{-1}$)	—	134.6% (10 000)	38.98	404.36	1 M KOH	122
25	K/Cl	$[K]^+$/$[Cl]^-$ doped Co-$(OH)_2$	112.1 F cm^{-2} ($5\ mA\ cm^{-2}$)	60.7% ($50\ mA\ cm^{-2}$)	98% (5000) at $50\ mA\ cm^{-2}$	39.8	478	6 M KOH	123

stability of TMHs. A series of studies on doping of metal ions have been carried out to stabilize $Ni(OH)_2$ and promote the capacitance of $Ni(OH)_2$. Fu's team[47] synthesized the flower-shaped Zn-doped $Ni(OH)_2$ electrode (Zn doped $Ni(OH)_2$@CNTs) using a colloidal synthesis method, assisted by cetyltrimethyl ammonium bromide (CTAB) and $NaBH_4$. A hybrid supercapacitor (HSC) assembled using the Zn doped $Ni(OH)_2$@CNTs as the positive electrode and active carbon as the negative electrode exhibits a capacity of 201.7 C g^{-1} at 1 A g^{-1} and an energy density of 51.3 W h kg^{-1} at a power density of 409.6 W kg^{-1} (Table 1, entry 3).

Zhao *et al.*[48] used a heterogenous Zn element doped in nickel-based hydroxide, which greatly optimized the inherent electronic structure and conductivity. Besides, the introduction of porous reduced graphene oxide (rGO) substrate with excellent conductivity can not only greatly accelerate the electron transfer between the collector and hydroxide but also inhibit the agglomeration of hydroxide. Thanks to the introduction of a sandwich structure, rGO and Zn doping, this Ni–Zn hydroxide/rGO material has obtained abundant contact sites and high conductivity. This SC material features suitable capacitance (615.4C g^{-1} at 1 A g^{-1}), appropriate stability (87.5% after 8000 cycles), and superior capacity rate property (62.3% retention at 30 A g^{-1}) (Table 1, entry 4).

Chen *et al.*[49] demonstrated that the robust and high output Zn doped NiOOH–FeOOH (Zn–$Fe_xNi_{(1-x)}$OOH@NF) catalyst can be reconstructed by Zn-doping and electrooxidation. Dynamic reconstruction of Zn–(Ni/FeOOH)@NF under the oxidizing condition was revealed by a series of *in situ* Raman and *ex situ* characterizations. Zn modification to Ni only occurred in the form of the NiZn alloy rather than doping to NiO. In addition, the electron transfer from Zn to Ni can optimize the electronic property of Ni nanoparticles, improving their catalytic performance. Consequently, the reconstructed

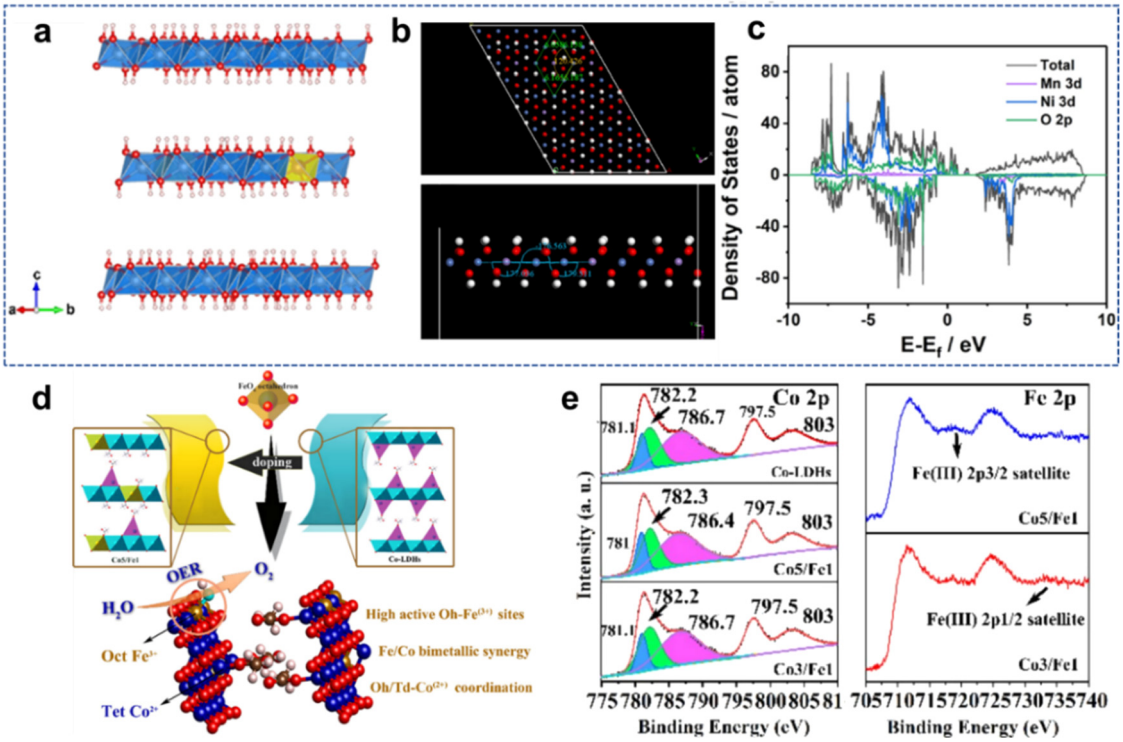

Fig. 4 (a) Side view of the optimized supercell model with an interlayer distance of 7.9 Å (blue: Ni; yellow: Mn; red: O; white: H). (b) Supercell model and side view of the optimized second layer. (c) The total electronic densities of state (TDOS) of NiMn-LDH materials. Reproduced with permission from ref. 46 © 2021 Elsevier B.V. (d) Abstract of Fe^{3+} doping cobalt-based hydroxide nanosheets (e) Co 2p and Fe 2p XPS spectra of Fe^{3+} doping cobalt-based hydroxide nanosheets. Reproduced with permission from ref. 55 © 2021 American Chemical Society.

Zn–$Fe_xNi_{(1-x)}$OOH@NF electrode exhibited a low overpotential for the high-output OER (η_{1000}= 330 mV, and η_{1500}= 347 mV) and showed tiny performance degradation after a 1000 h stability test at 1000 mA cm^{-2} (Table 2, entry 1).

3.1.3. Al-doped LSHs. Song's group developed a novel strategy to prepare flower-like Al-doped Ni(OH)$_2$ with different Ni^{2+}/Al^{3+} molar ratios.[50] Al doping changes the morphology of LSHs and increases specific surface area, so the structure stability and electrochemical performance of Al-doped Ni(OH)$_2$ are significantly improved (Table 1, entry 5). However, Al does not participate in faradaic redox reactions for energy storage, so the specific capacitance of this LSH decreases.

In contrast, Al^{3+}-doped α-Ni(OH)$_2$ has a better capacitance since Al doping can cause low crystallinity and high crystal defects. Yang *et al.*[51] successfully synthesized another Al^{3+}-doped α-Ni(OH)$_2$ with flower-like morphology and porous structure through a simple one-pot hydrothermal method. This material displays an ultra-high specific capacitance of 1750 F g^{-1} at 1 A g^{-1} and a good electrochemical stability of 72% after 2000 cycles of operation. In addition, the assembled asymmetric supercapacitor with this material as the positive electrode exhibits a high energy density (49.6 W h kg^{-1} at 573.8 W kg^{-1}) (Table 1, entry 6).

3.1.4. Fe-doped LSHs. Boettcher's group[52] has identified Ni(Fe)OxHy is an active OER catalyst in alkaline media. To further investigate the OER activity enhancement by Fe doping,[53] a series of metal cations including Ti^{4+}, Mn^{2+}, La^{2+}, and Ce^{4+} are doped into $Ni_{(1-z)}M_zO_xH_y$ to evaluate their OER activities and effects on $Ni^{2+/3+}$ oxidation potential in an alkaline solution. The comparison indicates that only Ce enhances the OER activity of NiO_xH_y, but the enhancement is much less than Fe. These results highlight the curial roles of Fe in the OER and confirm that Fe is the active site of the OER in Ni(Fe)O_xH_y.

Wang *et al.*[54] introduced Fe-doped α- and β-Ni(OH)$_2$ for H_2O splitting. Compared with Fe-doped β-Ni(OH)$_2$, Fe-doped α-Ni(OH)$_2$ is more conducive to forming the higher valence Fe sites, which are the major active centers in the OER. In contrast, Fe doping in the β phase may enhance the electron density of Fe sites, thereby facilitating the adsorption of H atoms to accelerate the HER process. Only a 53.8 mV overpotential for Fe-doped β-Ni(OH)$_2$-240 is required to achieve a current density of 10 mA cm^{-2} (Table 2, entry 2). Therefore, Fe-doped β and α-Ni(OH)$_2$ are used as the cathode and anode, respectively, in battery hydrolysis, which has high H_2O splitting efficiency.

Liu *et al.*[55] reported that Co^{2+} occupancy and coordination in cobalt-based LDH nanosheets can be tuned *via* Fe^{3+} doping. (Fig. 4(d)). It is found that the appropriate incorporation of Fe^{3+} can greatly activate the originally inactive octahedral coordinated Co^{2+} centers, which promotes the overall electrocatalytic activity of Co-based LDHs (Fig. 4(e)). Density functional theory (DFT) calculations also clarify that Fe^{3+} not only regulates the configuration of Co^{2+}, but also acts as additional catalytic active sites. Therefore, the optimized LDH nanosheets

Table 2 Summary of HER/OER catalyst performance

Entry	The doped heteroatom	Catalyst/substrate	Electrochemical: Overpotential (mV) (@10 mA cm^{-2}) HER	OER	Cell voltage (@10 mA cm^{-2})	Tafel slope (mV dec^{-1}) HER-OER (mV dec^{-1})	Stability (@10 mA cm^{-2})	Ref.
1	Zn	Zn–(Ni/FeOOH)@NF	—	269 (100 mA cm^{-2})	—	33	1000 h at 1000 mA cm^{-2}	49
1	Fe	Fe-doped Ni(OH)$_2$/NF	53.8	208	1.54 V	79.37–45.54	20 h at 20 mA cm^{-2}	54
2	Fe	Co/Fe LDH/	—	285	—	44.6	4 h	55
3	Fe	NiFe-LDH@NF	—	328 (50 mA cm^{-2})	—	31.1	10 h at 50 mA cm^{-2}	56
4	Mn	Mn-doped NiFe(OH)$_2$	—	194	—	52	—	61
5	Ce	Fe:Ni(OH)2/ FeCe:Ni–(OH)2/NF	—	201	—	42.4	50 h	63
6	Ce	Ni–Fe–Ce-LDH	—	242	—	34	24 h	64
7	Zn	PA-ZnFeCo LDH	—	221	—	58.73	10 000 s	67
8	Zn	Zn; NiFeOxHy	—	250	—	28.3	24 h	68
9	Fe	Fe–CoNi LDHs	—	260	—	49	12 h	70
10	Fe	Fe-doped NiCo-LDH	—	285	—	62	16 h	71
11	Fe	Fe–CoMo UH	—	245	—	37	90 h	72
12	Fe	$Ni_3V_1Fe_1$-LDH	—	269	—	67	—	73
13	W	(NiFeW-LDHs	—	211	—	36.44	120 h	74
14	Ta	Ta–NiFe LDH	—	260 (50 mA cm^{-2})	—	58.95	20 h at 100 mA cm^{-2}	75
15	Cr	CoFeCr LDH/NF	—	202	—	83	20 h	76
16	Cr	Cr-CoFe LDHs/NF	—	238	—	107	20 h	77
17	V	PV-NiFe LDH NSA	19	295 (100 mA cm^{-2})	1.43 V	38–58	1000 h	78
18	V	$Co_2Fe_{0.5}V_{0.5}$		242	—	41.4	20 h	79
19	V	NiFeV LDHs.	—	195 (20 mA cm^{-2})	—	42	18 h 98%	80
20	V	NiFe-V	—	254	—	37	20 h	81
21	S	S-doped $Ni_{4/5}Fe_{1/5}$-LDHs	—	257	—	61.5	30 h	86
22	P	P-doped MoO_3/ FeCo-LDH/NF	—	225	—	87.4	80 h	91
23	N	N-CoFe LDHs	—	233	—	40.03	—	95
24	F	F-doped NiFe-LDH	—	225	—	79	10 h	99
25	F	F–NiAl LDH NF	—	330	—	53	12 h	100
26	F	F-doped α-Ni(OH)$_2$	—	325	—	31.89	30 h	101
27	F	F-NHO	—	280	—	107	24 h 91.3% at 20 mA cm^{-2}	102
28	Cl	Cl-doped Co(OH)$_2$	—	330	—	98	12 h	103
29	NO_3^-	Co–Al LDH–NO_3^-	—	223	—	102	—	110
30	DS^-	DS^- doped Co(OH)$_2$ NCs	—	561	—	172	—	42
31	$[MoS_4]^{2-}$	MoS_4-LDH/NF	91	—	1.37 V	125	24 h	115
32	POM	NiFe LDH-POM/NF	200	156	1.6 V	86–67	20 h	116
33	B/P	NiVFe-B-P LDH@NF	117	—	—	68	24 h	121
34	Y/P	YP-Co(OH)F	55	238	1.54 V	52–67	300 h	124
35	Mn/F	Mn–F/Ni(OH)$_2$–NF	—	233 (20 mA cm^{-2})	—	56.9	10 h at 20 mA cm^{-2}	125

(Co : Fe molar ratio is 5 : 1) show the lowest overpotential of 285 mV and the smallest Tafel slope of 44.6 mV dec^{-1} (Table 2, entry 3).

Dong *et al.*[56] prepared Fe doped NiFe-LDH nanosheets and investigated in depth the influence mechanism of Fe doping by controlling the Ni/Fe ratio and the Fe valence state. Fe doping can control the structure morphology and promote the oxidation of Ni^{2+}, making the electrode have a low overpotential of 382 mV at 50 mA cm^{-2}, and the low gradient of Tafel is 31.1 mV dec^{-1} (Table 2, entry 4).

In order to improve the overall performance of nickel hydroxide and cobalt hydroxide in terms of specific capacitance and charge–discharge rate, mixed metal hydroxide seems to be better than single metal hydroxide. Doping foreign elements in LSHs can introduce an intermediate band, which has a profound impact on the band gap and electron energy of LSHs. Meanwhile, the molar ratio of active divalent metal ions to trivalent metal ions has a sensible impact on the structure, morphology and capacitive performance of LSHs.

3.2. Double metal-hydroxides (LDHs)

LDHs are types of 2D anionic clay with the structural formula $[M_{(1-x)}^{2+}M_x^{3+}(OH)_2]^{x+}[(A^{n-})_{x/n}\cdot yH_2O]_x$. In the presence of OH^-, the divalent cation M^{2+} in the $M(OH)_6$ brucite-like structure is partially replaced by the trivalent metal cation M^{3+}, forming a positively charged 2D host layer, while the anion A^{n-} balances the charge in the middle of the layer (Fig. 5).[27] The structure of LDHs can be greatly modified by changing the M^{2+}/M^{3+} molar ratio or the category of A^{n-}. Meanwhile, the nanostructures of LDHs offer greater functions by having hierarchical structures with large active surface areas, tailoring the distribution of materials homogeneously along the structure, the interconnected structure, or combining the advantages of tunable organic–inorganic components and controllable thickness at the nanoscale-all for the goal of maximizing the properties.[57,58] For example, in 2010 Yan *et al.* assembled a positively charged LDH monolayer with a cationic functional molecule (BNMA) by using polyanions (PVS) as intermediates. This method allows

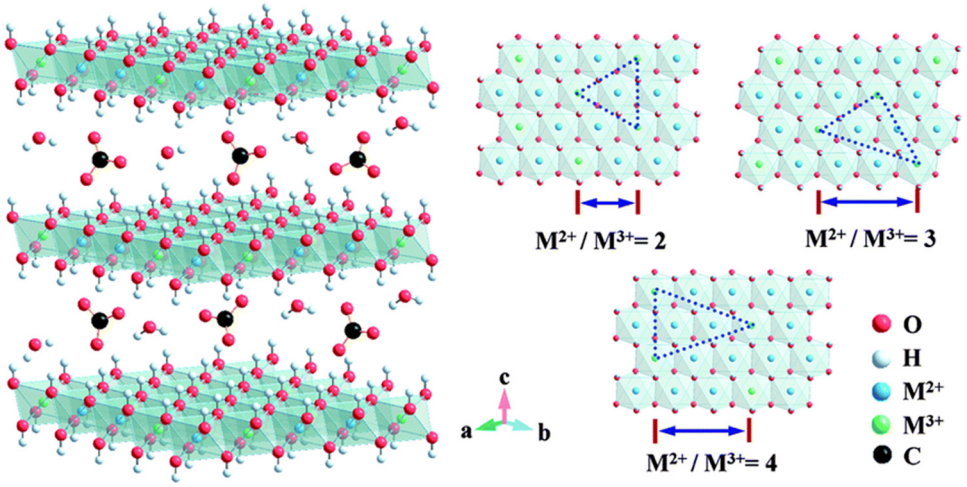

Fig. 5 The structure of carbonate intercalation LDHs with different M^{2+}/M^{3+} molar ratios. Metal hydroxide octahedrons are stacked along the crystalline *c*-axis, and water and anions are present in the interlayer region. Reproduced with permission from ref. 27 © 2014 The Royal Society of Chemistry.

fine-tuning and ordered assembly of functional cations and LDH monolayers for designing and achieving novel organic–inorganic ultra-thin films.[17] However, the original LDHs show low conductivity and severe accumulation, which reduce active sites and hinder the transport of electrolyte ions.[29] In addition, the 2D structure of LDHs is often deteriorated under harsh electrochemical conditions, which ultimately limits their electrochemical activity.

To overcome these problems, doping active metal cations (such as Mn^{2+}, Ce^{3+} Fe^{2+}/Fe^{3+}, Zn^{2+}, Ta^{5+}, V^{5+}, and Cr^{3+}) into the LDHs structure can increase the inherent conductivity to significantly improve the electrochemical activity. Furthermore, the doped additional metal cation can stabilize the valence of the primary metal ions of LDH and optimize their electronic structure, which protects a single component from oxidation to enhance the structure stability of LDH.[59,60]

3.2.1. Mn-doped LDHs. When Mn is used as a dopant, it can bring about hybridization between M 3d and O 2p orbitals, which is conducive to the oxidation of metal ions. Du *et al.*[61] investigated the effects of Mn doping on the electronic structure of NiFe LDHs and OER performance. DFT calculations suggest that Mn doping causes hybridization between the Ni 3d and O 2p orbitals to promote Ni^{2+} oxidation (Fig. 6(a)). X-ray absorption spectroscopy results also confirm that Mn doping stimulates the formation of high valence Ni^{4+} sites which are the main active sites for water oxidation. 5% Mn doped NiFe LDH exhibits an overpotential of 194 mV at 10 mA cm^{-2} in 1 M KOH and a Tafel slope of 52 mV dec^{-1} (Table 2, entry 5).

Wu *et al.*[62] synthesized Mn doped $Ni(OH)_2$ for urea electrooxidation (UOR). They confirmed by Raman spectroscopy that Mn dopants promoted the formation of electroactive NiOOH at low potential and extended the Ni–O bond in NiOOH, resulting in increased phase structure disorder. Mn doping can reduce the starting potential of nickel hydroxide oxidation, which is conducive to the generation of electrochemically active $Ni^{III}OOH$, making it have excellent UOR performance.

3.2.2. Ce-doped LDHs. Due to the special valence electron structure of rare earth elements, they can be used as co-catalysts. LDH doped with rare earth elements can combine the advantages of rare earth elements and LDH. Zhan *et al.*[63] synthesized Ce doped NiFe-LDH nanosheets with a highly-efficient catalytic performance in the OER. Ce doping enhances the electronic/ionic conductivities of NiFe-LDH, thereby improving its OER kinetics. Simultaneously, Ce induces the vertical arrangement of new nanosheets of 2D NiFe-LDH in the reaction, which increases catalytically active sites and intrinsic activity. Ce-doped NiFe-LDH displays an overpotential of 201 mV and a Tafel slope of 42.4 mV dec^{-1} in an alkaline electrolyte at a current density of 10 mA cm^{-2} (Table 2, entry 6).

Yan *et al.*[64] reported hollow 3D LDH microcapsules (Ni–Fe–Ce-LDH) for the OER by Ce ion doping (Fig. 6(b)). Ce ions possess excellent properties of multivalence, flexible coordination, and high affinity for hard oxygen donors. Therefore, Ce ion doping can play a key role in stabilizing a particular crystalline phase and modifying the electronic properties. Because, from the perspective of energy, the Ce dopant is likely to occupy the MIL-88A aperture structure and enhances electronic transfer by the Ce-4f band modulation with d–f couplings. These results show that the Ce dopant plays a vital role in structural transitions and effective OER. Consequently, Ni–Fe–Ce-LDH has outstanding OER activity, with an overpotential of 242 mV at 10 mA cm^{-2} and a long-term durability of $\geq$24 h (Table 2, entry 7).

Cao *et al.*[65] designed a La/Ce doping strategy to improve the OER performance of CoFe LDH. Because the ionic radii of La^{3+} and Ce^{3+} are much larger than Fe^{3+} and have unique electronic structures, La^{3+} or Ce^{3+} partially replaces Fe^{3+}, CoFe LDH system has more defects, which elevates electrocatalytic activity and abates oxygen evolution potential. Moreover, the partial replacement of Fe^{3+} will affect the electronic structure of CoFe LDH, enhancing the electronic coordination in the system and showing excellent OER performance.

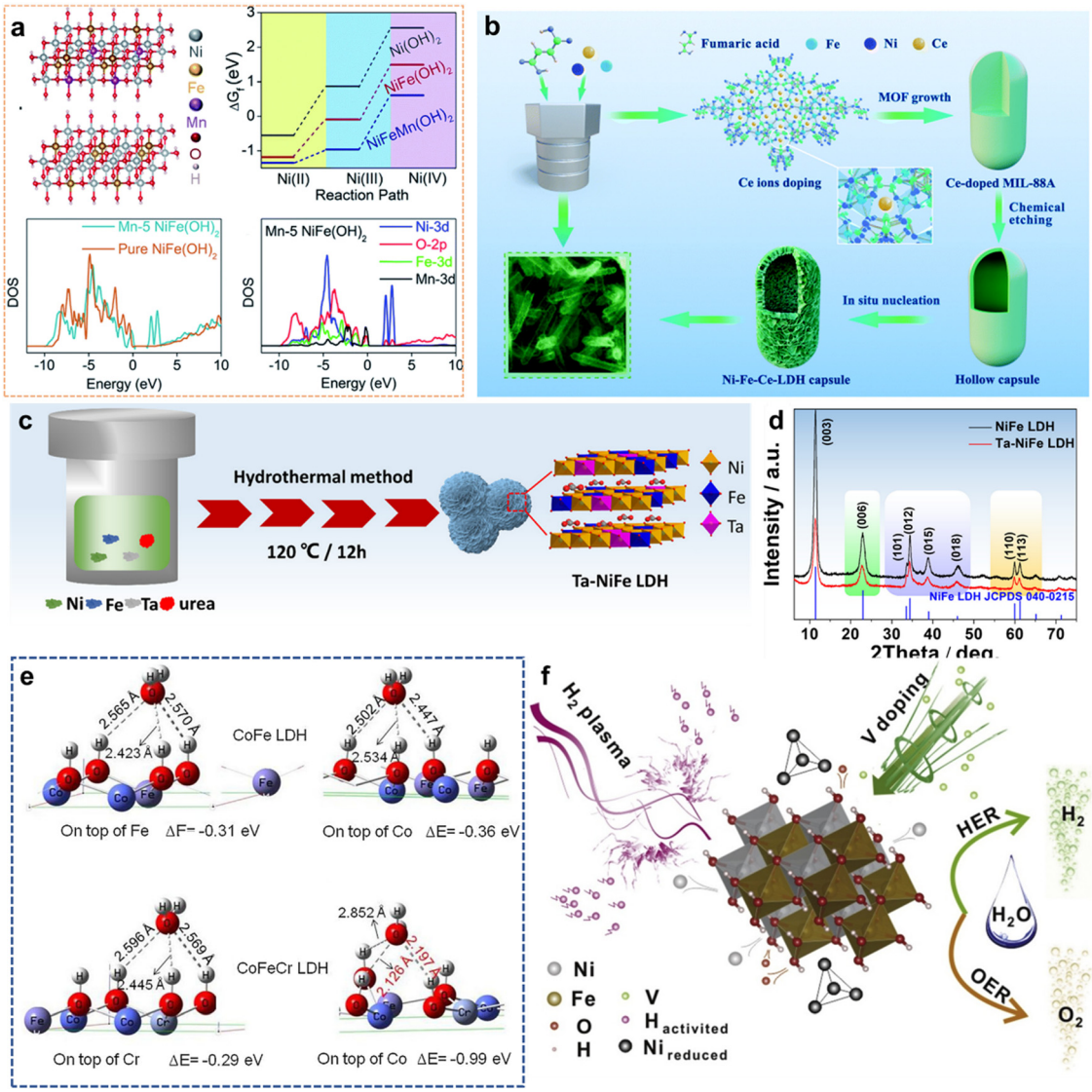

Fig. 6 (a) DFT+*U* calculation for the oxidation of Ni(II) and Ni(III) ions. Reproduced with permission from ref. 61 © 2020 The Royal Society of Chemistry. (b) Schematic illustration of the synthesis of hollow Ni–Fe–Ce-LDH microcapsules mediated by Ce doping. Reproduced with permission from ref. 64 © 2020 The Royal Society of Chemistry. (c) Schematic of preparing process of Ta–NiFe LDH; (d) The XRD patterns of NiFe LDH and Ta–NiFe LDH. Reproduced with permission from ref. 75 © 2020 Elsevier B.V. (e) The adsorption energies for H_2O on top of Fe sites and Co sites of CoFe LDH and Cr and Co sites of CoFeCr LDH. Reproduced with permission from ref. 76 © 2020 Elsevier B.V. (f) Schematic diagram of the structure of PV-NiFe LDH NSA. Reproduced with permission from ref. 78 © 2020 Elsevier B.V.

Duan *et al.*[66] utilized Ce doping to modulate the electronic structure of CoFe LDH and improve the conductivity in order to improve the performance of the exchange membrane water electrolyzer. At the same time, excessive Ce doping leads to the formation of an active interface between CeO_2 and CoFeCe-LDH, forming a self-assembled heterostructure CeO_2/CoFeCe-LDH interface, further enhancing the OER activity and increasing the turnover frequency.

3.2.3. Zn-doped LDHs. Zn doping makes a synergistic effect between Zn^{2+} and the host metal, improving the conductivity and intrinsic activity of the electrodes. Dong *et al.*[67] reported an inert Zn doped FeCo LDH (PA-ZnFeCo LDH) for high-efficiency OER. XPS analysis demonstrates that Zn doping may induce the emergence of Co^{3+} with more price 3d electron orbits on the surface of LDH, resulting in better electron-accepting capacity, which is favorable for the adsorption of OER intermediates, with overpotentials of only 221, 276, and 294 mV to drive 10, 100, and 300 mA cm^{-2} in 1.0 M KOH, respectively, and electrochemical stability of 100 000 s (Table 2, entry 8).

Zn can be used as a strong Lewis acid that causes partial charge transfer and electron delocalization around Fe sites. Nam *et al.*[68] disclosed a Zn-doped $NiFeO_xH_y$ catalyst (Zn–$NiFeO_xH_y$) for H_2O oxidation. As a dopant, therefore, Zn–$NiFeO_xH_y$ exhibits superior electrocatalytic activity and stability compared with $NiFeO_xH_y$. At a current density of 10 mA cm^{-2},

the overpotential of Zn–$NiFeO_xH_y$ is increased to 250 mV (Table 2, entry 9).

Zheng *et al.*[69] doped a small amount of inactive monovalent element Zn into NiCo LDH through two consecutive electrodepositions. Slight doping Zn^{2+} significantly improves the cycle performance of LDH, and the polyaniline (PANI) nano layer is used as the intermediate layer to enhance the interface interaction between LDH and the collector. The composite electrode achieved the best performance with a high specific capacitance of 1749 F g^{-1} and an ultralong life span with 89% capacitance retention after 40 000 charge–discharge cycles (Table 1, entry 7).

3.2.4. Fe-doped LDHs. The empty orbit and lone pair electrons of Fe^{3+} will attract electrons from other active centers around, which adjust the position of the center of the active metal d band. Consequently, Fe doping is capable of optimizing the adsorption strength between the active center and the reactant, reducing the binding energy between the reactant and the catalytic active site in the OER process. Liu *et al.*[70] used CoNi LDH as the matrix to introduce Fe^{3+} into the surface through cation exchange. This method makes the Fe sites mainly exist in the surface layer and edge of the nano sheet to expose more reaction sites. Due to the change in local structure and electronic properties, the overpotential of FeCoNi LDH is only 260 mV at 10 mA cm^{-2} (Table 2, entry 10).

Yamauchi *et al.*[71] used Ni–Co glycerate spheres as a self-template to induce the formation of porous Fe-doped NiCo-LDH nanosheets, confirming Fe doping could accelerate the hydrolysis rate of the spheres. These porous nanosheets with high specific surface areas increase active sites, and the synergistic effects of doped Fe and the main metal (Ni and Co) may improve the OER kinetics of this catalyst. Therefore, the Fe-doped NiCo-LDH exhibits a low overpotential of 285 mV and a low Tafel slope of 62 mV dec^{-1} at a current density of 10 mA cm^{-2} in OER (Table 2, entry 11).

Gu *et al.*[72] reported an effective strategy for synthesizing amorphous Fe-doped cobalt-molybdenum hydroxide (named Fe–CoMo UH) nanosheets. Benefiting from the ultrathin amorphous structure and multi-metal regulation, the Fe–CoMo UH nanosheets display outstanding OER performance, with a low overpotential (245 mV), a low Tafel slope (37 mV dec^{-1}) at 10 mA cm^{-2}, and excellent stability (Table 2, entry 12).

Li's team[73] reported the preparation of Fe^{3+} doped NiV-LDH ultra-thin nanosheets by one-step coprecipitation. Fe doping can adjust the valence state of Ni sites, giving Ni^{3+} a higher oxidative capability. In addition, the presence of Fe^{3+} in NiV-LDH effectively promotes its charge transmission. Hence, $Ni_3V_1Fe_1$ LDH shows excellent catalytic activity in the OER process. In 1.0 M KOH solution, the ultrathin $Ni_3V_1Fe_1$-LDH nanosheet only needs a low-output level of 269 mV to achieve a current density of 10 mA cm^{-2} and also has a cycle stability of 1000 times as the electrode (Table 2, entry 13).

3.2.5. Ta/W-doped LDHs. The introduction of high valence elements in LDH can not only modulate the electronic structure but also is a feasible strategy for generating oxygen vacancies (V_O).[74] Yamauchi's team reported W-doped NiFe-LDHs nanosheets with V_O which are directly deposited on Ni foam (NF) *via* an electrodeposition method combined with a chemical corrosion engineering strategy. An appropriate amount of W doping will locally modulate the electronic structure environment of Ni and Fe and gradually increase the concentration of V_O. Oxygen vacancies effectively decorate the intrinsic electronic structure of NiFe LDHs, optimize the adsorption energy of intermediate products, and thus form rich OER electrocatalytic active centers on the surface of the electrocatalyst. The representative $NiFeW_3$-LDHs exhibit remarkable OER electrocatalytic activity with a low overpotential (211 mV at 10 mA cm^{-2}), a small Tafel slope (36.44 mV dec^{-1}), and fine stability (more than 120 h at 10 mA cm^{-2}) (Table 2, entry 14).

Zhang *et al.*[75] employed high-valence Ta to dope a NiFe LDH catalyst to enhance H_2O oxidation (Fig. 6(c)). According to XRD analysis in Fig. 6(d), Ta doping causes LDH lattice expansion. XPS analysis indicates that there is electronic interaction between Fe and Ta (electron transfer from Fe to Ta). Meanwhile, Ta doping is conducive to the adsorption of OH^- on the Ta sites to reduce overpotential and improve the electrocatalytic activity in the OER. The optimized Ta–NiFe LDH displays excellent OER activity, with a low overpotential of 260 mV and a small Tafel slope of 58.95 mV dec^{-1} at a current density of 50 mA cm^{-2} (Table 2, entry 15).

3.2.6. Cr-doped LDHs. As one of the primary dopants, Cr atoms with a high valence state can adjust the electronic structure of active center atoms. The electronic structure of the active center atom is adjusted, which reduces the band gap, improves the electronic conductivity, and increases the electrochemical active center. Recently, Li *et al.*[76] introduced a Cr doped CoFe-LDH as an efficient, strong, dual-function electrocatalyst for the OER and oxidation of urea (UOR). During the OER, Cr^{3+} may be partially oxidized to a high valence state (Cr^{6+}) with a strong electron-withdrawing property, modifying the electronic structure and stabilizing the active sites. DFT calculations show that the Cr doping effectively adjusts the electron density of the active sites (Co sites), thereby effectively overcoming H_2O adsorption during oxidation in Fig. 6(e). Therefore, CoFeCr LDH/NF shows considerably enhanced electrocatalytic performance, with an ultra-low overpotential, low Tafel slope and satisfactory stability in alkaline media (Table 2, entry 16).

Similarly, Li *et al.*[77] prepared a kind of OER catalyst by introducing Cr dopants into CoFe LDHs (Cr-CoFe LDHs/NF) using a simple one-step hydrothermal method. DFT calculations indicate that Cr dopants could improve the electron-donation ability owing to the electronegativity differences between Cr and Co/Fe, which significantly tune the adsorption energy among four oxygen intermediates, increasing the activity of OER. This Cr-CoFe LDHs/NF catalyst has a superior overpotential of 238 mV at 10 mA cm^{-2} and high electrochemical durability for 20 h (Table 2, entry 17).

3.2.7. V-doped LDHs. As shown in Fig. 6(f), Yu *et al.*[78] combined cation doping and a plasma reduction strategy for the preparation of multiple vacancies V-doped NiFe-LDH nanosheets (PV-NiFe LDH NSA). Both V doping and O vacancies reduce the energy barrier of O* in the OER, and the synergy

effects of V sites, O and Ni vacancies expose more active centers and superior electron transfer pathways (Table 2, entry 18).

Zhang's group[79] applied V doped CoFe LDH to improve the OER activity. DFT calculations indicate that V doping could increase the M–O bond energy within the LDH and promote charge transfer from O to metals. The $Co_2Fe_{0.5}V_{0.5}$ catalyst exhibits an overpotential of 242 mV at 10 mA cm^{-2} in the OER under alkaline conditions, with a Tafel slope of 41.4 mV dec^{-1} (Table 2, entry 19).

Sun *et al.*[80] synthesized a series of V doped NiFe LDH nanosheets array (denoted as NiFeV LDHs) *via* a one-step hydrothermal method for OER electrocatalysis. DFT+*U* simulation suggests that the high catalytic activities of the NiFeV LDHs are mainly attributed to the V doping, which alters the electronic structure and narrows the band gap, thereby improving conductivity and facilitating electron transfer. A small overpotential of only 195 mV to drive a current of 20 mA cm^{-2}, with a low Tafel slope of 42 mV dec^{-1}, in a 1.0 M KOH solution (Table 2, entry 20).

Liu *et al.*[81] introduced different V contents in the process of synthesizing NiFe LDH to adjust the surface electronic structure and valence state of NiFe LDH, enhancing the electron transfer and electrochemically active surface area of LDH to further improve the intrinsic electrocatalytic activity. Compared with undoped NiFe LDHs, the oxygen evolution overpotential of NiFe-V decreases by 37 mV, and the Tafel slope decreases by 43.37 mV 10 mA cm^{-2} (Table 2, entry 21).

After the above discussion, we found that doping additional redox flexible metals in LDH can increase the number of active centers of the OER by improving the synergy between the nearest adjacent metal atoms. Therefore, compared with mono-active metal or bi-active metal hydroxides, doping metal elements to construct multi-active metal hydroxides may also provide a better utilization of the electroactive sites due to their homogeneous elemental distribution.

4. Non-metal doping

Recently, anion engineering received widespread attention as a strategy to modify the electrical activities of TMHs.[30] As shown in Fig. 7(a), the cation provides a strong positive electric field when the anion is not polarized, which favors OH^- adsorption but not O_2 adsorption. Conversely, the polarized anion exhibits the covalent character of allowing electrons to enter the empty orbital of the cation, promoting the interaction. However, when over-polarized, the positive electric field is weakened, and the hydroxyl group is not completely adsorbed. Therefore, the regulation of the electronic structure to generate appropriate polarization can promote covalent and ionic interactions between cations and anions, thereby promoting electron transfer, adsorption, and desorption.[82]

In addition, the anion engineering may also influence the hydrogen bonding nature in the interlayer space of TMHs. As a representative example (Fig. 7(b)),[83] the embedding of high negative atom F^- may weaken the hydrogen bond between the OH^- structural group and the host ions in the interlayer space. In addition, the anions with larger diameters perhaps to expand the intermediate layer space of LDHs, which may expose more active sites and promote electron transport.

4.1. S doping

The NiV-LDH prepared by Huang's group displayed a high specific capacitance, but poor stability.[84] Therefore, they further proposed an effective strategy to improve the stability of NiV-LDH by S doping. Compared with that of the original NiV-LDH, the cycle stability of NiV-S is much higher (NiV-S exhibited a retention rate of 98.5% after 10 000 cycles) (Table 1, entry 8).

To further simplify the S-doping process, Zhu *et al.* designed a one-step hydrothermal method for preparing S-doped NiCo-LDH as a high-performance asymmetric capacitor.[85] As shown in Fig. 7(c), the morphology of NiCo-LDH is changed by controlling the amount of S. S incorporated into the crystal lattice may decrease the crystallinity of the material and induce low-oxidation-state Ni species (Fig. 7(d)). In addition, the introduced S impurities may effectively tune the electronic structure of NiCo-LDH, increasing its inherent conductivity. Compared with that of the original NiCo-LDH, S-doped NiCo-LDH-S7.5 exhibits a unique nanosheet spherical structure, thus exposing more active sites and improving contact with the electrolyte. The assembled supercapacitor electrode exhibits an extremely high energy density of 73.54 W h kg^{-1} at a power density of 375 W kg^{-1} and great cycle stability (Table 1, entry 9).

Li *et al.*[86] reported a simple method to construct an S-doped NiFe-LDH electrocatalyst for the OER, as shown in Fig. 7(e). The S doping could regulate the adsorption energy of OH* and O* on the Fe sites, accelerating the OER process. Moreover, the synergy of S and Fe sites improves the activity of the catalyst, and the amount of S doping also influences the OER activity of the NiFe-LDHs. The optimal S-doped $Ni_{4/5}Fe_{1/5}$-LDH catalyst displays excellent OER performance with an overpotential of 257 mV at 10 mA cm^{-2}, a Tafel slope of 61.5 mV dec^{-1}, and excellent stability (Table 2, entry 22).

Niu *et al.* prepared a kind of S-doped $Ni_2(OH)_2CO_3$@MWCNT nanocomposites through a one-step hydrothermal method.[87] XPS analysis illustrates that there is an electronic interaction between S and $Ni_2(OH)_2CO_3$, so the assembled asymmetric supercapacitor (ASC) displays an energy density of 45 W h kg^{-1} and wonderful cycle stability (Table 1, entry 10).

4.2. P doping

The electronegativity of P is lower than those of O and S. Doping low-electronegativity species may also increase the conductivity of semiconductor catalysts, leading to faster electrochemical kinetics.[88,89]

For example, P-doped CoNi-LDH can optimize the conductivity and electronic structure, which improves the catalytic performance in the methanol oxidation reaction (MOR).[90] Xiao *et al.* used NaH_2PO_2 as the P source to generate P-CoNi-LDHs with different forms coupled with reduced graphene oxide (rGO) *via* cyclic voltammetry deposition. The structure–activity

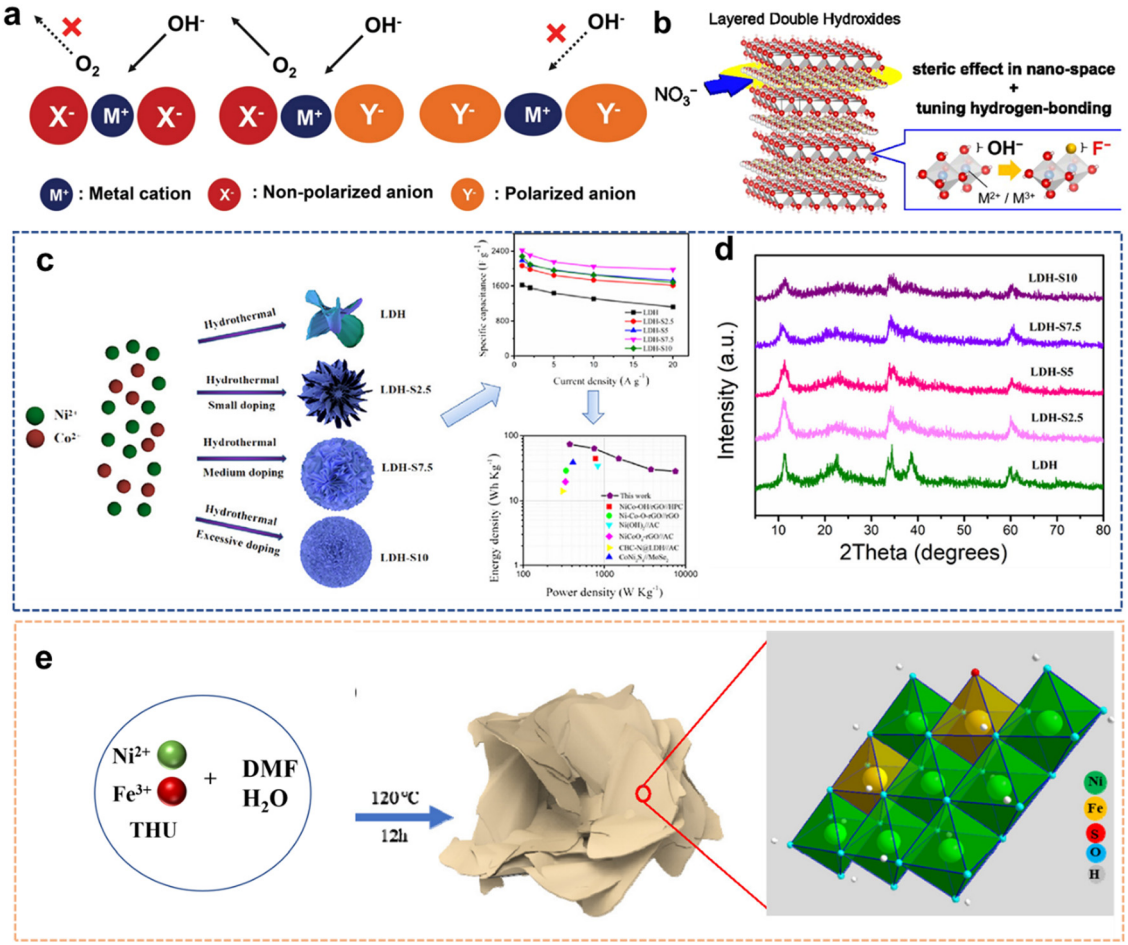

Fig. 7 (a) Schematic of anion regulations by optimizing the electronic structure of active sites toward water oxidation. Reproduced with permission from ref. 82 © 2017 Wiley-VCH Verlag GmbH & Co. KGaA, Weinheim. (b) Crystal structure and schematic image of fluorine substitution of a brucite-like layer of LDHs. Reproduced with permission from ref. 83 © 2019 American Chemical Society. (c) Gradual changes in the morphology of the LDH-S electrode material and corresponding electrochemical properties. (d) XRD patterns of the LDH-S. Reproduced with permission from ref. 85 © 2020 American Chemical Society. (e) Schematic illustration of the synthetic of the $Ni_{4/5}Fe_{1/5}$-LDHs-S-2. Reproduced with permission from ref. 86 © 2020 Dalian Institute of Chemical Physics, Chinese Academy of Sciences.

relationship analysis demonstrates that P doping improves the electronic structure and conductivity of this material and increases the MOR activity which is twice that of the original CoNi-LDH.

Huan *et al.*[91] prepared a 3D P-doped MoO_3/FeCo-LDH/NF ultrathin nanosheet heterostructure electrocatalyst for a high-efficiency OER. The heterostructure between P-MoO_3 and FeCo LDH not only optimizes the electronic structure but also induces electron transfer. Moreover, the substitution of Mo^{6+} in MoO_3 with P can stabilize the O vacancies, thereby providing superior conductivity and more active sites. P-MoO_3/FeCo-LDH/NF exhibits significant OER catalytic activity in alkaline media, with a very low overpotential of 225 mV at a current density of 10 mA cm^{-2}, and an excellent durability of $\geq$80 h (Table 2, entry 23).

Mei *et al.*[92] synthesized P-doped NiCoZn LDH/NF through typical hydrothermal and calcination methods. P doping can reduce the adsorption energy of H, promoting desorption, and improving the corresponding catalytic activity. When PeNiCoZn LDH/NF-15% is used as the anode and cathode for urea-water electrolysis, the voltage is 1.479 V for urea-water electrolysis at 100 mA cm^{-2}.

4.3. N doping

Plasma technology is a powerful method for surface etching and N doping.[26,93,94] Wang *et al.* utilize N_2 plasma treatment to peel off a large amount of CoFe-LDH, producing N-doped ultrathin CoFe-LDH nanosheets.[95] N doping can change the electron density of adjacent metal atoms, which favors the formation of adsorption intermediates in the OER. Simultaneously, the exfoliated ultrathin CoFe-LDH nanosheets possess more atomic-sized holes and edge regions, thus exhibiting outstanding OER performance with overpotentials of 233 mV at a current density of 10 mA cm^{-2} (Table 2, entry 24).

Kang *et al.* exfoliated a NiAl-LDH layer using N_2 plasma to obtain mono or dual layer nanosheets.[96] Nitrogen plasma can remove CO_3^{2-} anion layers and form abundant oxygen vacancies on the surface of LDH. N doping can replace a portion of

oxygen vacancies in the lattice to form metal–N and N–O bonds. In addition, with the help of doping nitrogen, oxygen vacancies promote the adsorption of the oxidation intermediate. Hence, both oxygen vacancies and nitrogen doping increase charge carrier density and reduce charge transfer interface resistance, thereby promoting water oxidation kinetics.

Mei *et al.*[97] fabricated an N-doped NiZnCu LDH with rGO on Ni foam as an electrocatalyst of the HER. First, NiZnCu-LDH/rGO is synthesized by a hydrothermal method, and then, N-doping is achieved *via* calcination under NH_3 gas. The unique morphology of N–NiZnCu LDH/rGO exposed numerous active sites, resulting in excellent catalytic activity. For ammonia oxidation reaction (AOR), UOR and hydrazine oxidation reaction (HzOR) at current densities of 10 mA cm^{-2}, the voltages of these materials are 0.489, 1.305, and 0.010 V, respectively, with excellent stabilities (over 3000 cyclic voltammetry cycles).

4.4. F doping

The fluoride anion has the strongest electronegativity (4.0) and a similar anion diameter with O.[98] Therefore, F doping may tune the electronic structure of metal sites in the TMHs and form M–F bonds, which accelerate the inherent electron transfer rate of TMHs.

For example, Feng's group found that F doping can enhance the OER performance of FeNi LDH.[99] XPS spectra disclose that F doping causes the modification of the electronic structure and the formation of Fe–F bonds in the FeNi-LDHs. The conversion from the M–O bonding to the M–F bonding after F-doping is significant for the OER owing to the facile formation of metal (oxy)hydroxide over the surface. F-doped NiFe-LDH exhibits a low overpotential of 225 mV at 10 mA cm^{-2}, with a Tafel slope of 79 mV dec^{-1} (Table 2, entry 25).

Similarly, Xi *et al.*[100] synthesized an F-doped NiAl LDH as an efficient OER catalyst. The catalytic activity of F–NiAl LDH is almost 10-fold stronger than that of the undoped catalyst. This is because the strongly electronegative F^- is conducive to building weak M–F bonds, which easily break to form the active species of nickel oxides/hydroxides, thereby enhancing OER catalytic performance (Table 2, entry 26).

Xu *et al.*[101] reported a novel strategy for fabricating F-doped α-$Ni(OH)_2$ mesoporous 2D ultrathin nanosheets for H_2O splitting and multifunctional electrodes in supercapacitors (Fig. 8(a)). In Fig. 8(c), the pink strip reveals the contribution of the F atom. Compared to Ni and O atoms, the peak of the F atom is weak. However, the presence of F atoms alters the coordination environments of Ni and O and further produces a new peak near the Fermi level. In addition, several bands that appear near the Fermi level and the lower Gibbs energy of the OER prove that F doping can improve conductivity (Fig. 8(d)). Therefore, the F-doped α-$Ni(OH)_2$ nanosheets exhibit excellent electrocatalytic activity and stability with a low onset potential (260 mV) and Tafel slope (31.89 mV dec^{-1}) in the OER (Table 2, entry 27). In addition, this material can be used in supercapacitors with high specific capacitances of 158.75 F g^{-1} at 1 A g^{-1} (Table 1, entry 11).

Jiang's team[102] prepared F doped Ni oxyhydroxide (F-NHO) mesogenic microspheres as high-efficiency electrocatalysts for the OER. F^- is incorporated into the Ni oxyhydroxide lattice to form Ni–F bonds with enhanced ionic properties, which stabilize the Ni(III) species, achieving a higher electronegativity difference between Ni and F. Meanwhile, F^- incorporation can enhance the electrochemical durability and resistance to harsh alkali and oxidation conditions under high potential, resulting in higher catalytic efficiency in the OER during H_2O electrolysis (Table 2, entry 28).

4.5. Cl doping

As shown in Fig. 8(e), Zhong *et al.*[103] introduced Cl^- into $Co(OH)_2$ to grow Cl-doped $Co(OH)_2$ on carbon cloth as an integrated electrode. According to the experimental results, Cl in the electrocatalyst can be oxidized to destroy the internal structure of the catalyst and introduce defects. The Cl-doped $Co(OH)_2$ nanosheets with defective structures exhibit improved electrocatalytic OER activities owing to their larger electrochemical surface areas (Table 2, entry 29).

Hou *et al.*[104] prepared Cl-doped cobalt carbonate hydroxide ($Co(CO_3)_{0.35}Cl_{0.20}(OH)_{1.10}$) nanowires for supercapacitors. The unique nanowire structure formed by Cl doping can increase the hydrophilicity and enable deep electrolyte ion diffusion, thereby reducing internal resistance. The prepared nanowires display excellent capacitances (9893.75 F g^{-1} at 0.5 A g^{-1}) and energy densities (220 W h kg^{-1}), cycle stability up to 10 000 cycles (Table 1, entry 12).

In general, when these non-oxygen anion dopants enter the TMHs lattice, they induce changes in the charge density of the metallic body of the TMHs and fine-tune the chemical interactions. The synergistic effect of the dopant produces critical changes in the physical and chemical properties. Importantly, multicomponent hybrid TMHs promote synergistic effects, which reduce the adsorption energy of adsorbates (OH*, OOH*) and enhance overall conductivity. In short, combining TMHs with other components leads to multiple oxidation states and protects the individual components to improve the electrochemical performance of TMH-based nanomaterials under long-term processes against severe corrosion conditions.

4.6. Interlayer intercalation

The ''layers'' of the LDHs exhibit unique properties. The host layers provide a flexible confined space to accommodate various guest anions, which result in host–guest interactions such as electrostatic interactions, hydrogen-bonding. When specific non-organic or other anionic groups are applied to insert or replace the anion A^{n-} of the LDHs, the characteristics of the ''layers'' are altered, which has a significant effect on the physical and chemical properties of the LDHs.[105,106]

4.6.1. Inorganic ions. Generally, the intercalation ions are mostly inorganic ions with small diameters (CO_3^{2-}, NO_3^-, and Cl^-). For example, Wu *et al.*[107] electrochemically synthesized nickel hydroxide nanoparticles *in situ* doped anion using different nickel salt solutions. During cathode deposition, NO_3^-, CO_3^{2-}, or SO_4^{2-} can be inserted into $Ni(OH)_2$ *in situ* to

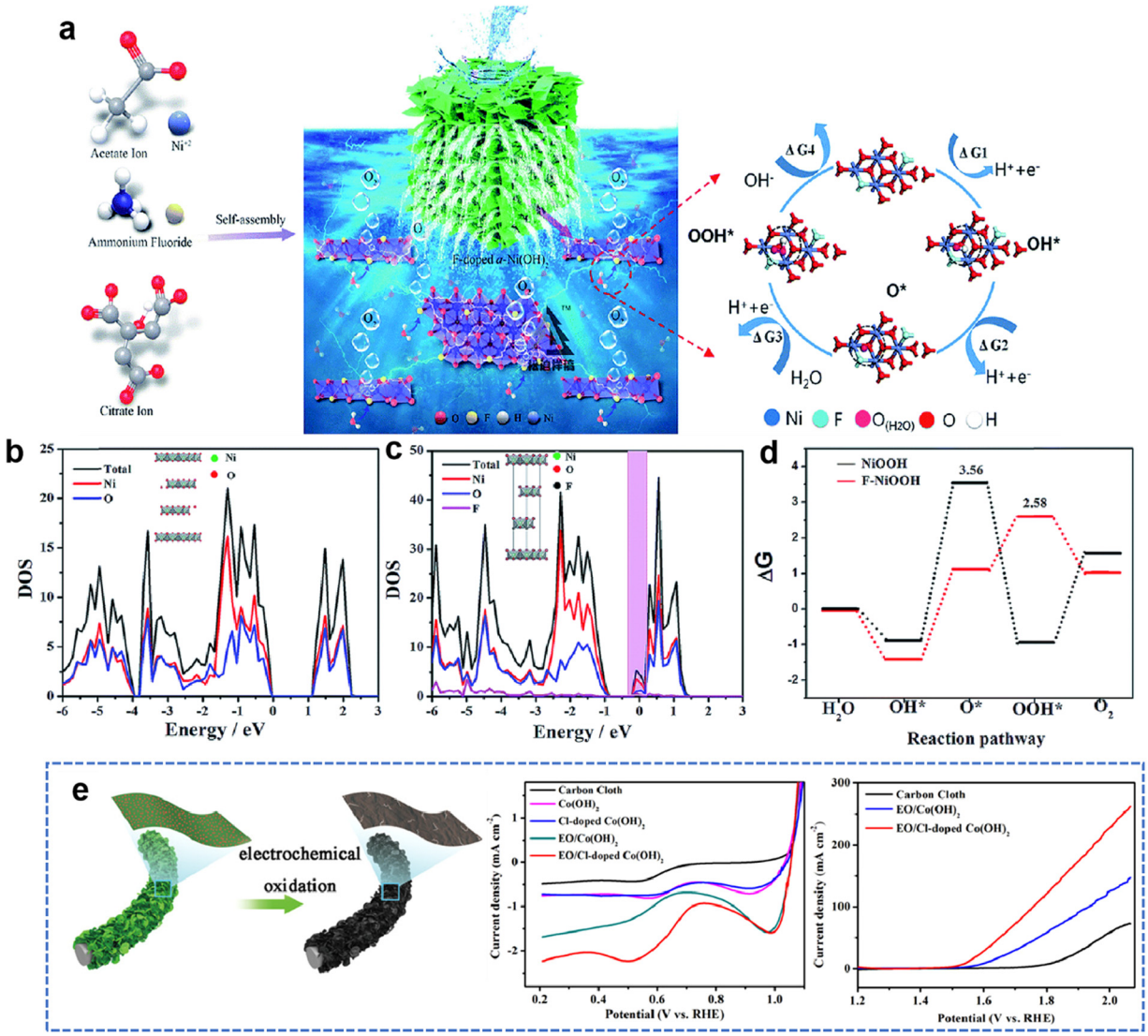

Fig. 8 (a) Schematic illustration of the synthesis of ultrathin mesoporous F-doped α-$Ni(OH)_2$ nanosheets and their application for efficient water splitting. (b) Density of states of NiOOH. (c) Density of states of F–NiOOH. (d) Standard free-energy diagram of the OER process of NiOOH and F–NiOOH. Reproduced with permission from ref. 101 © 2019 The Royal Society of Chemistry. (e) Schematic of Cl-doped $Co(OH)_2$ and electrochemical properties. Reproduced with permission from ref. 103 © 2017 American Chemical Society.

form the α-phase, whereas CH_3COO^- cannot be inserted into $Ni(OH)_2$. The electrochemical performances of the prepared $Ni(OH)_2$ electrodes are investigated by cyclic voltammetry (CV) and galvanostatic charge–discharge tests. The interlayer anions are embedded to increase the interlayer spacing, which significantly improves the electron transfer. The sample with inserted NO_3^- exhibits the highest electrochemical performance compared with those of the samples with inserted SO_4^{2-} or Cl^- and β-$Ni(OH)_2$ (Table 1, entry 13).

Kim *et al.*[108] developed a homogeneous precipitation method to prepare an α-$Ni(OH)_2$ intercalated with dodecyl sulfate (α-Ni–$(OH)_2$-DS). Subsequently, anion exchange was carried out to insert desired anions (Cl^-, NO_3^-, AcO^-, SO_4^{2-}) without any change in morphology. α-$Ni(OH)_2$ embedded with a smaller radius Cl^- exhibits the largest specific capacitance in this series (Table 1, entry 14). Because Cl^- ions are singly charged and fabulous hydrophilic, the exchange and transport of OH^- ions are more facile. However, the doubly charged anions such as SO_4^{2-} prevent OH^- ion and water to enter the surface of $Ni(OH)_2$, consequently, leading to low specific capacitance.

Wang *et al.*[109] reported that Co-MOF as a template composited with different manganese salt solutions to form CoMn-LDH with different anion intercalations (Fig. 9(a)). Due to the effects of different anion metal salts, the synthesized LDH contains different layer spacing. At the same time, the MOFs can better control the 3D porous structure and increase the specific surface area. Among these LDHs, CoMn-LDH-SO_4 has the largest lattice spacing and highest surface area, which exhibits the optimal supercapacitor performance, with an area capacity of 582.07 mC cm^{-2} and an energy density of 0.096 mW h cm^{-2} at a power density of 1.5 mW cm^{-2} (Table 1, entry 15).

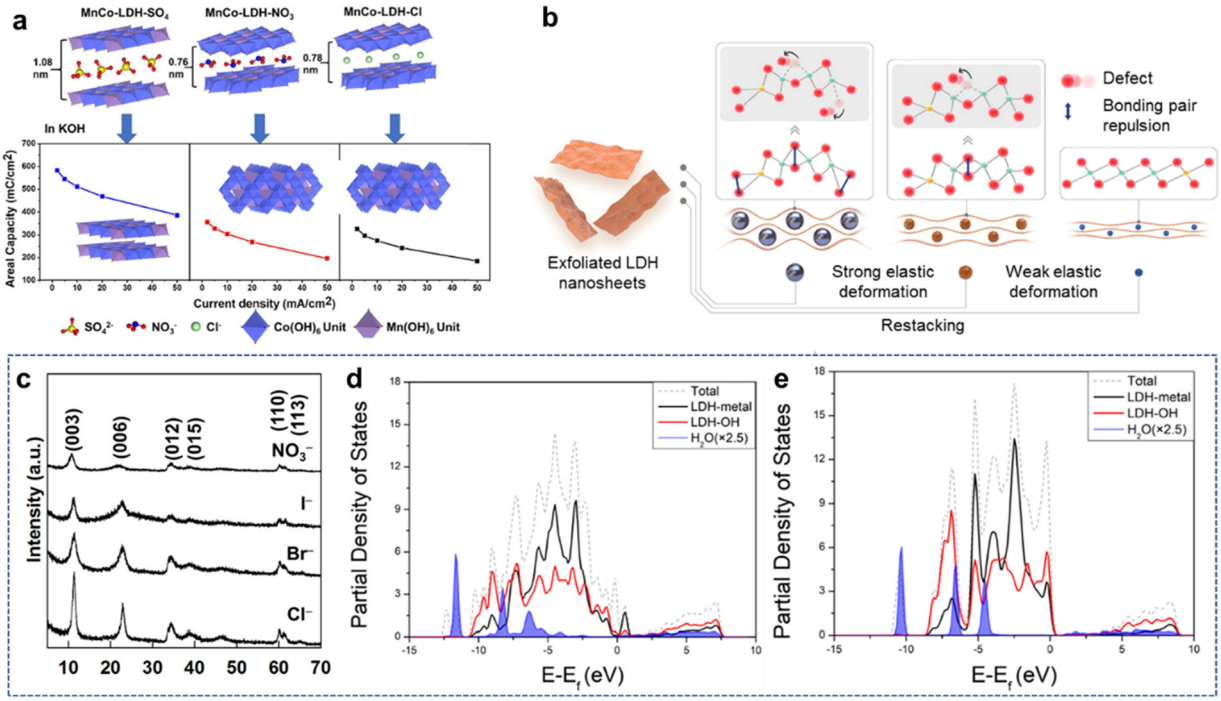

Fig. 9 (a) Schematic of the synthesis of CoMn-LDH. Reproduced with permission from ref. 109 © 2019 American Chemical Society. (b) Schematic diagram for defect and stacking control of LDH NSs. (c) XRD pattern, (d) PDOS of Co–Al-LDH with an oxygen defect and (e) without an oxygen defect. When a water molecule develops a close interaction with metals for the Co–Al-LDH system with an oxygen defect, the PDOS of water is significantly broadened, in particular, for the occupied states. Reproduced with permission from ref. 110 © 2021 American Chemical Society.

Kim *et al.* prepared CoAl-LDH nanosheets (LDH NSs) with variable stacking and pore structures by adjusting the size of the intercalator.[110] A series of Na salts with different anions (Cl^-, Br^-, I^-, and NO_3^-) are applied to restack the LDH NSs. The restacking and the embed of anions lead not only to an increase in the substrate spacing but also to significant elastic deformation of the peeled LDH NSs in Fig. 9(b) and (c). Lattice engineering simultaneously controls the number of stacks and O vacancies by tuning the size of the intercalator. DFT calculations reveal that the increase in the layer spacing will change the electrostatic potential in the lattice, which modifies the reducibility of Co^{3+} sites and directly affects the nearby O vacancy formation (Fig. 9(d) and (e)). Therefore, the defect-rich Co–Al-LDH-NO_3^- nanohybrid with a small stacking number displays excellent performance as an OER electrocatalyst (Table 2, entry 30) and a supercapacitor electrode (Table 1, entry 16).

Guo's team[111] suggests that the structural stability of α-$(Ni/Co)(OH)_2$ can be enhanced by introducing the inherent column effect of metaborate. The embedded metaborate pillars can be firmly bonded in the intermediate layer of the Ni–Co hydroxide, which stabilizes the structure of the electrodes, resulting in excellent cycle performance. At a current density of 5 A g^{-1}, the average capacitance decay rate of the metaborate-stabilized α-$(Ni/Co)(OH)_2$ is only ~0.0017% after 10 000 cycles (Table 1, entry 17).

All in all, anion insertion may expose more active sites, while the unique interlayer spaces in the catalytic process also avoid the loss of these active substances, thereby effectively improving the activity of the catalytic system. More importantly, the insertion of the guest anion into the LDH intermediate layer generates an attraction between the cation and guest anion, which may alter the stacking number or stack thickness or porosity of the layers.

4.6.2. Large diameter organic ions. The most obvious feature of doping large diameter ions is that it can expand the layer spacing of LDHs. Because larger interlayer space can promote faster charge storage kinetics and enables the structure to be retained during the reaction.[88]

Yang *et al.*[112] studied the effects of the average interlayer spacing on the capacitance of NiMn LDHs. The layer spacing of NiMn LDHs is controlled (from 7.38 to 28.41 Å) by adding different amounts of sodium lauryl sulfate, while the morphology and composition are unchanged. The capacitance correlates positively with the average layer spacing of NiMn-LDH. NiMn-LDH4 with the largest interlayer spacing exhibits the highest specific capacity of 325 mA h g^{-1} at a current density of 1 A g^{-1} (Table 1, entry 18).

Qiu *et al.*[42] enhanced the activity of layered cobalt hydroxide nanosheets as the H_2O oxidation catalyst by adjusting the interlayer spacing. At first, dodecyl sulfate (DS^-) inserted cobalt hydroxide is prepared. NO_3^- or CH_3COO^- inserted cobalt hydroxide NCs are then synthesized *via* anion exchange. When these three cobalt hydroxides are used as OER electrocatalysts in neutral phosphate-buffered saline, DS^- inserted cobalt hydroxide induces the largest interlayer spacing and highest activity (Table 2, entry 31).

Zhang *et al.*[113] used sodium oleate as a surfactant and an intercalant to prepare NiAl-LDH (NA-LDH-OA) nanosheets. The enlarged interlayer space and 2D frame structure could provide an effective pathway for ions and electron transmission, enhancing the electrochemical activity. Therefore, the assembled ASC device (NA-LDH-OA-2//AC) exhibited a high energy density of 40.26 W h kg^{-1} at a power density of 943 W kg^{-1} and maintained a good cycle performance of 94.5% after 5000 cycles (Table 1, entry 19).

Yan *et al.*[114] used excess $Na_2C_2O_4$ as an oxalate source and an intercalator to introduce cobalt oxalate ions $[CoOx_2]^{2-}$ into the middle layer of $Co(OH)_2$ *via* a one-step solvothermal method to synthesize I-$Co(OH)_2$ NSs. The embedded column ions maintain the excellent structural stability of the nanosheets, thereby enhancing the electrical conductivity and accelerating Li^+ diffusion. As shown in Fig. 10(a)–(d), when the prepared I-$Co(OH)_2$ NSs are used as the liquid lithium battery anode material, they exhibit superior rate performance (566 mA h g^{-1} at 5 A g^{-1}) than that of undoped β-$Co(OH)_2$ NSs and excellent cycle stability (870 mA h/g at 1 A g^{-1} after 250 cycles) (Table 1, entry 20). Fig. 10(e) shows the optimized atomic structures of the I-$Co(OH)_2$ and $[CoOx_2]^{2-}$ interlayers. The functional density calculation manifests that the intercalation of $[CoOx_2]^{2-}$ leads to a higher dispersion of the band structure in $Co(OH)_2$, thereby improving the Li^+ diffusion kinetics and achieving high conductivity (Fig. 10(f)–(h)).

Kurungot *et al.*[115] reported that $[MoS_4]^{2-}$ was embedded into the interlayer space of NiCo-LDH *via* exchange with NO_3^-, forming an efficient catalyst material for urine to direct H_2 production. X-ray photoelectron energy spectroscopy and electrochemical analysis illustrate that the embedded $[MoS_4]^{2-}$ not only adjusts the interlayer spacing but also alters the overall electronic structure of NiCo-LDH, thereby reducing the internal potential and resulting in favorable kinetics for the HER. When this catalyst is used as a cathode and anode to produce a urea electrolytic cell, only ~1.37 V cell potential is required to generate sufficient H_2 and maintain long-term catalytic efficiency by reaching the benchmark 10 mA cm^- in 1 M KOH/0.33 M urea. (Table 2, entry 32).

Liu's team[116] applied $K_8[SiW_{11}O_{39}]\cdot 13H_2O$ heteropoly acid as a hydrolysis and structural orientation agent to insert into NiFe LDHs, forming a 3D NiFe LDH-POM nano-flower-like structure, which was an efficient dual-functional catalyst for overall H_2O splitting. Compared with the original NiFe LDH, W^{6+} alters the electronic structure of the active center, which minimizes the adsorption energy barrier of HO*, thereby improving the

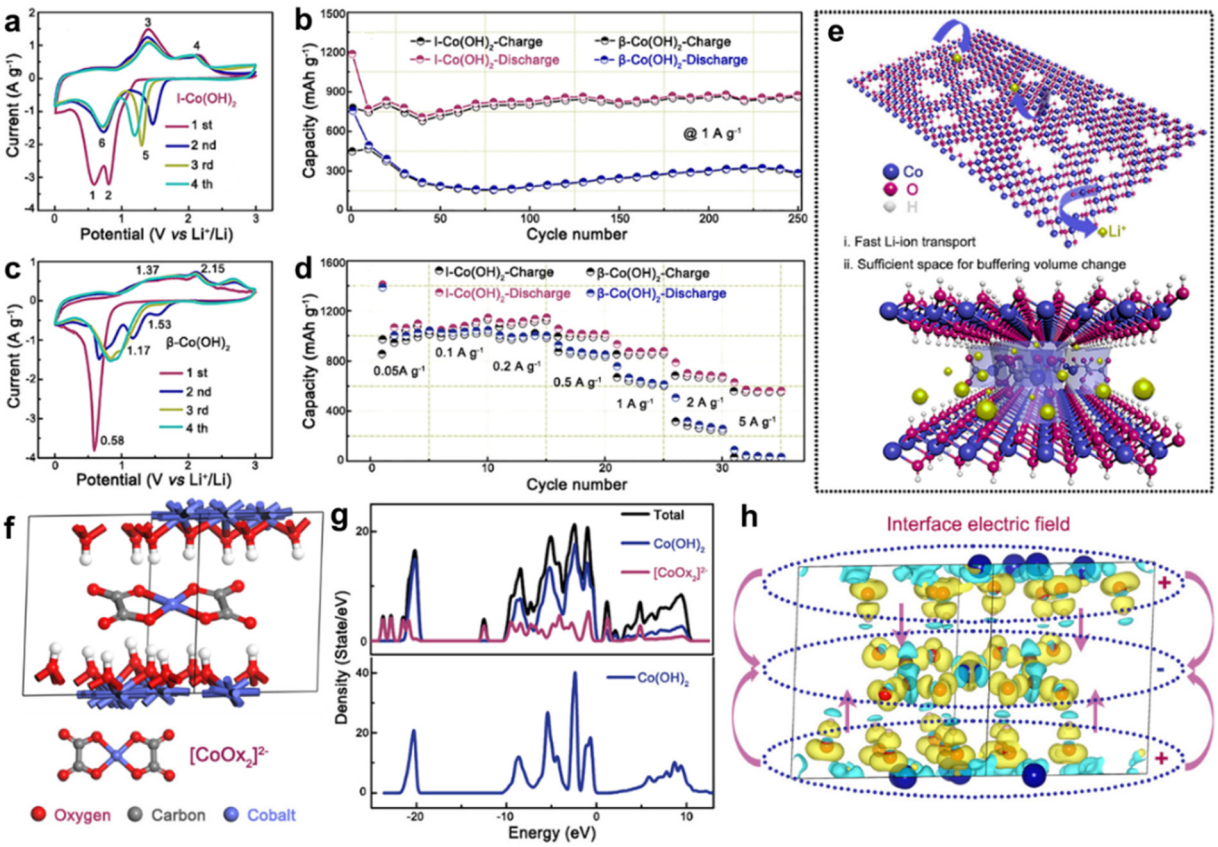

Fig. 10 Lithium-ion storage properties and electronic structure calculations of I-$Co(OH)_2$ and β-$Co(OH)_2$ NSs. (a and b) CV curves for the first four cycles. (c) Cycling performance and (d) rate capabilities. (e) Schematic illustration highlights the structural benefits of the anode during Li-ion diffusion. (f) Optimized atomic configurations, (g) density of states, and (h) charge-density difference. Reproduced with permission from ref. 114 © 2018 American Chemical Society.

kinetics of the OER. The as-prepared catalyst achieves overall water splitting current density of 10 mA cm^{-2} at low overpotentials (OER: ~200 mV; HER: ~156 mV) in 0.1 M KOH over a period of 20 h operation (Table 2, entry 33).

Hence, LDHs are ideal supports for the immobilization of active species such as the large diameter active ions. Anions with larger embedded radii may expand the interlayer spaces of the LDHs, which can form an appropriate layer spacing to attenuate the resistance of the LDHs' active component interaction with OH^-.[83] The facile electron transfer will facilitate the deprotonation/protonation reaction, achieving fast kinetics and thus high electrochemical performance.

5. Co-doping

A suitable dopant should show an ideal modulation effect on the host material, but sometimes a single dopant does not satisfy all requirements. Generally, further co-/multi-doping is required to enhance the advantages of heteroatom doping.[32] Thus, for the co-doping strategy, we should not only consider the physical characteristics and theoretical requirements of the co-dopant but also confirm whether it may have a positive synergistic effect in TMHs under non-equilibrium growth conditions.

5.1. Metal co-doping

The first choice of co-dopant may be two cations. Various multimetal hydroxides can be prepared by two cations. Yuan *et al.*[117] prepared Cu^{2+} and Ni^{3+} co-doped $Ni(OH)_2$, using a simple one-step co-precipitation, which is an anode material of high-capacity, long-life Li-ion batteries. Cu^{2+} doping changes the nucleation conditions of $Ni(OH)_2$ and increases the interlayer spacing, thereby promoting the migration of Li^+ electrons and increasing the stability of the layered structure. Simultaneously, Cu^{2+} promotes the *in situ* generation of Ni^{3+}, which improves the capacitances of $Ni(OH)_2$. Therefore, the co-doped $Ni(OH)_2$ exhibits an excellent lithium storage capability with an ultra-high first-discharge capacity of 1832.5 mA h g^{-1} at 0.2 A g^{-1}. The reversible capacities reach 1230.1 mA h g^{-1} and 942.5 mA h g^{-1} after 800 and 1000 cycles at a rate of 1 A g^{-1} and 2 A g^{-1}, respectively (Table 1, entry 21).

Fan *et al.*[118] prepared α-$Ni(OH)_2$/graphene with co-doped metal ions (Al^{3+} and Co^{2+}) by a co-precipitation approach. According to XRD analysis, Al^{3+} doping causes the phase to transform from β-$Ni(OH)_2$ to α-$Ni(OH)_2$ while Co^{2+} doping makes the interlayer distance of α-Ni(OH) increase. Due to its large interlayer distance, mesoporous structure and highly conductively graphene, the Al–Co co-doped α-$Ni(OH)_2$/GNS (Al–Co–Ni/GNS) displays excellent specific capacitance (2257 F g^{-1} at 2 mV s^{-1}) (Table 1, entry 22).

5.2. Non-metal co-doping

The co-doping strategy of two or more anion ions is also very common in the modification of TMHs.[119] Kim *et al.* developed an S and P co-doping strategy to enhance the electrocatalytic activity and supercapacitor performance of NiCo-LDH.[120] S and P co-doping can regulate the morphology of NiCo-LDH nanoarray (NiCo-LDH-SP). The heterogeneous porous structure effectively reduces charge transfer resistance, which achieves a rapid and efficient Faraday reaction. The assembled NiCo LDH-SP//AC supercapacitor behaves high energy density of 74.5 W h kg^{-1} at a power density of 0.8 kW kg^{-1} and maintains approximately 81.3% of the initial specific capacitance after 5000 cycles (Table 1, entry 23).

Chen's group[121] prepared a self-supporting B and P co-doped NiVFe LDHs@NF electrocatalyst for the HER. B-P co-doping formed numerous defects and amorphous regions on the nanosheets to ensure effective active sites and increase active surface area. In addition, the self-supporting structure enhances superhydrophilic and superhydrophobicity, which facilitates the electrolyte to enter the electrocatalyst, thereby promoting the occurrence of the HER. NiVFe-B-P LDH@NF exhibits excellent HER performance, with a low overpotential of 117 mV and a Tafel slope of 68 mV dec^{-1} at a current density of 10 mA cm^{-2} in a 1 M KOH electrolyte solution (Table 2, entry 34).

Zhu *et al.*[122] employed egg whites as a heteroatom-doping precursor to prepare a sandwich structure of C and N co-doped nickel hydroxide/nickel sulfide (C/N–$Ni(OH)_2$/Ni_xS_y). C-doping may improve the conductivity and cycle stability, and N-doping may expose more active sites, which enhances interactions between electrolytes and electrodes. The unique sandwich structure effectively prevents the reunion of $Ni(OH)_2$ nanosheets and Ni_xS_y nanoparticles. C/N–$Ni(OH)_2$/Ni_xS_y has an excellent capacitance of 1731.2 F g^{-1} at a current density of 0.5 A g^{-1}. The assembled C/N–$Ni(OH)_2$/Ni_xS_y//rGH supercapacitor displays a long-cycle performance and maintains 134.6% of the initial capacitance after 10 000 cycles at the current density of 5 A g^{-1} (Table 1, entry 24).

5.3. Metal and non-metal co-doping

At the same time, metal and non-metal co-doping can improve the selectivity of the TMHs doping strategy. To change the electronic and thermodynamic properties of $Co(OH)_2$, Xie *et al.* developed a K^+/Cl^- doped $Co(OH)_2$.[123] DFT calculations reveal that the substitution of OH^- with Cl^- can increase the adsorption energy for OH^- and H_2O to reduce the penalty originating from the coulombic repulsive interaction between hydrogen atoms of OH^- and of $Co(OH)_2$. At the same time, K replaces Co in the framework, which reduces the band gap to increase the conductivity (Fig. 11(a) and (b)). Electrochemical characterization confirms that the capacitances of K^+/Cl^--doped $Co(OH)_2$ are significantly enhanced (Fig. 11(c)–(e)). Compared with that of the original $Co(OH)_2$, the capacitances of K^+/Cl^--doped $Co(OH)_2$ are increased by 139.6%, and the contained supercapacitor presents an energy density of 39.8 W h kg^{-1} at a power density of 478.6 W kg^{-1}. (Table 1, entry 25).

Yang *et al.*[124] reported the synthesis of phosphorus and yttrium co-doped Co(OH)F (YP-Co(OH)F) nanorod arrays on nickel foam for overall water splitting. Experimental results demonstrated that the Y and P co-doping (YP-Co(OH)F) achieves the tuning of the electronic environment, which effectively

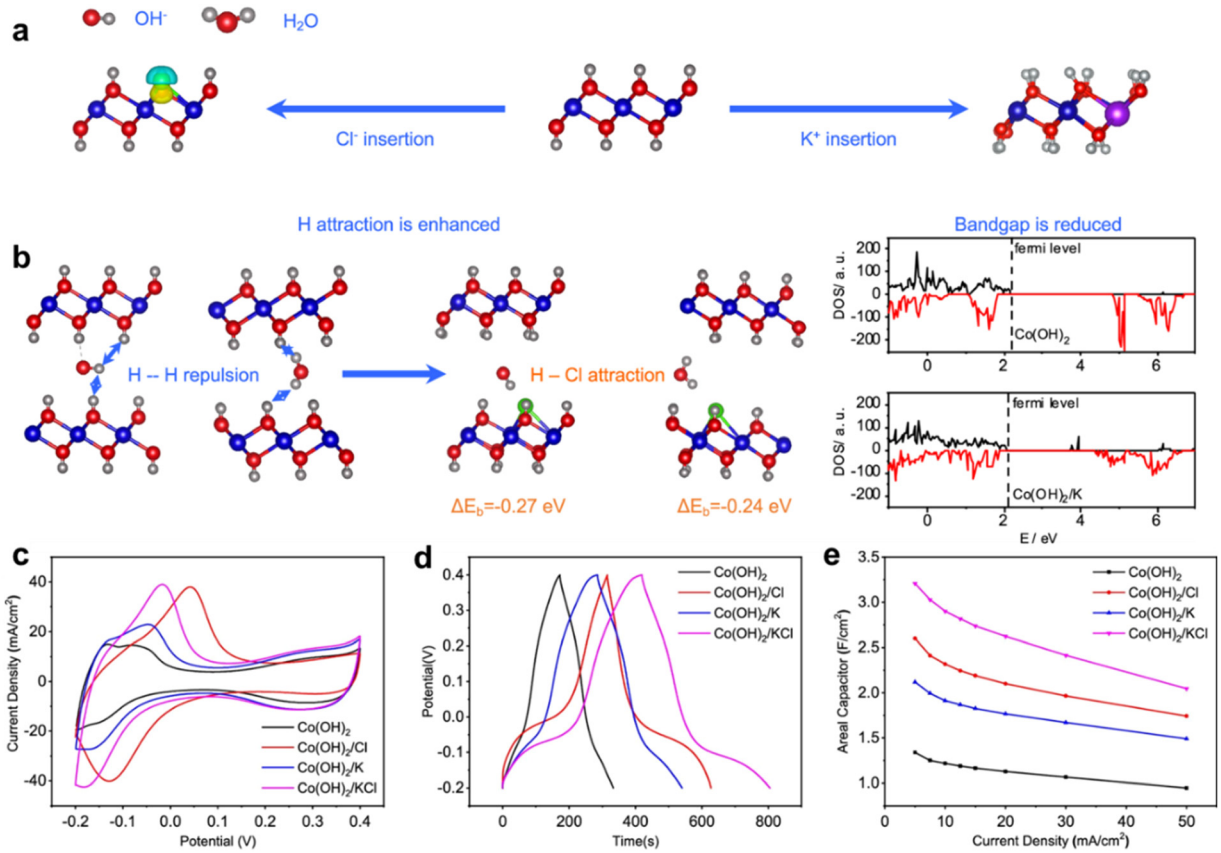

Fig. 11 (a) Schematic illustration view of K^+/Cl^--doped $Co(OH)_2$. (b) Cl^- doping can reduce the repulsive interaction between the inserted OH^- with $Co(OH)_2$ layers and the band gap properties of the K^+/Cl^--doped $Co(OH)_2$. Electrochemical performance of $Co(OH)_2$ with different modifications. (c) CV curves at 5 mV s^{-1}; (d) GCD curves at 5 mA cm^{-2}; (e) areal capacitances at different current densities. Reproduced with permission from ref. 123 © 2021 American Chemical Society.

reduces the charge transfer resistance in the catalytic reaction. C-doping Y and P also induces more active centers to be exposed, thereby the properties of catalysts in H_2O splitting are improved. The YP-Co(OH)F electrodes only required an overpotential of 238 mV to reach a current density of 10 mA cm^{-2} and exhibited an overpotential of 55 mV in the HER. When YP-Co(OH)F was used as the anode and cathode in a two-electrode structure, it only demands a cell potential of 1.54 V at 10 mA cm^{-2} and maintains stable water splitting for 300 h (Table 2, entry 35).

Li's team[125] successfully introduced Mn(III) into 2D F-doped $Ni(OH)_2$ to implement Mn and F co-doping strategies. The F atom has a high electrical negative property, and the doping can stabilize the structure of $Ni(OH)_2$. At the same time, the presence of F causes minimal changes in the Ni $(OH)_2$ internal structure, resulting in the loss of nearby oxygen atoms and generating vacancies on the surface of F/$Ni(OH)_2$. Then, with the further introduction of Mn(III), the electron repulsion of the nickel hydroxide changes, and the oxygen-deficient content increases. DFT calculations further suggest that the introduction of O defects can significantly improve the OER catalytic performance. Mn and F co-doped $Ni(OH)_2$–NF on Ni foam (Mn–F/$Ni(OH)_2$–NF) proves to be an efficient catalyst for the OER. In 1 M KOH electrolyte, Mn–F/$Ni(OH)_2$–NF has 233 mV overpotential at a current density of 20 mA cm^{-2}, and the Tafel slope is 56.9 mV dec^{-1} (Table 2, entry 36).

6. Summary and outlook

In summary, this study reviews the recent progress of heteroatom doping in TMHs with regard to energy conversion and storage applications. According to the structural characteristics of TMHs, the engineering of heteroatom doping is divided into metal doping, non-metal doping, and co-doping. The doping principles and effects of different elements are discussed. As emphasized in this review, this heteroatom doping strategy results in a great improvement in the electrochemical applications of TMHs. (1) Heteroatom doping can change the structure and morphology of TMHs, increasing the activity specific surface area and the stability of the capacitors. (2) It can regulate the electronic coordination environments of THMs, and improve the charge transfer kinetics of catalytic reactions. (3) It increases metal active sites to optimize electrocatalytic adsorption energy.

However, there are still several challenges limiting the doping engineering of TMH materials for energy conversion and storage applications: (1) there are no clear indicators on

how to select appropriate dopants to achieve the desired effect. (2) Whether diverse doping methods will have a hold on the role of dopants, and how to choose doping methods. (3) It is difficult to control the doped techniques to achieve positive effects, and it may also disrupt the original crystal structure, resulting in the performance degradation of TMH activity. (4) The basic understanding of the structure and performance relationship of doped TMHs is still not clear enough. (5) The effect of dopants on electrode performance is not clear enough so in-depth analysis and investigation of the doping effect and principles are highly demanded.

The existence of these challenges also provides the following opportunities for researchers in this field:

(1) The feasible dopants can be classified according to their own characteristics, such as low/high valence atoms, low/high electronegativity atoms, *etc.*

(2) According to the characteristics of selected dopants and substrate materials, appropriate doping methods are selected and the effects are compared. Calcination doping can produce more vacancies, and hydrothermal doping can expand the interlayer spacing.

(3) Researchers should perform doping engineering without interfering with the inherent activity of TMHs. The categories, quantities and positions of dopants should be carefully controlled to ensure the controllability of the doping technique to achieve positive effects. From the characterization perspective, synchronous radiation and aberration-corrected high resolution electron microscopy can provide more information on the categories, quantities and positions of dopants.

(4) Researchers should also pay attention to the relationship between the dopant and the structure of TMH itself. The mechanism of action of doped atoms varies with the structure and composition of TMHs. They should pay more attention to how to obtain real-time information on the doped sites during catalytic processes through *in situ* methods. Numerous *in situ* technologies (such as *in situ* XPS, *in situ* Raman, *in situ* FTIR, *in situ* XRD, *in situ* TEM–SEM) can be employed to disclose the reaction mechanism and structure–activity relationship, which can be further confirmed by DFT calculations.

(5) Researchers should follow with interest the role of dopants in electrochemical performance. After understanding the coordination mechanism of dopants to TMHs, we should compare their practical application as an electrode. The causation for the breakthrough of the electrochemical performance of doped TMHs was explored. Thereby, an optimal doping method is explored through minor changes to prepare the most effective heteroatom doped TMHs.

Author contributions

The manuscript was written by all the authors. All authors approved the final version of the manuscript. Guoping Lu, Yuxin Tang and Pengcheng Wang designed the outline and revised the manuscript. Yaqi Qin, Feng Yang, Chunhua Xu, Shuaijie Jiang, Yuqiu Wang are responsible for searching the literature, writing, and modifying the manuscript.

Conflicts of interest

There are no conflicts to declare.

Acknowledgements

This research was funded by the National Natural Science Foundation of China [Grant No. 11972195].

References

1 M. A. M. Khan and Y. I. Go, *Energy Storage*, 2020, **3**, 221–225.
2 C. Sun, J. Liu, Y. Gong, D. P. Wilkinson and J. Zhang, *Nano Energy*, 2017, **33**, 363–386.
3 P. Simon and Y. Gogotsi, *Nat. Mater.*, 2020, **19**, 1151–1163.
4 P. Ragupathy, S. D. Bhat and N. Kalaiselvi, *WIREs Energy Environ.*, 2022, **11**, 464.
5 C. Cao, F. Liang, W. Zhang, H. Liu, H. Liu, H. Zhang, J. Mao, Y. Zhang, Y. Feng, X. Yao, M. Ge and Y. Tang, *Small*, 2021, **17**, 2102233.
6 L. Yao, N. Zhang, Y. Wang, Y. Ni, D. Yan and C. Hu, *J. Power Sources*, 2018, **374**, 142–148.
7 Y. Gong, H. Zhao, D. Ye, H. Duan, Y. Tang, T. He, L. A. Shah and J. Zhang, *Appl. Catal., A*, 2022, **643**, 118745.
8 M. Li, K. Yang, M. Abdinejad, C. Zhao and T. Burdyny, *Nanoscale*, 2022, **14**, 11892–11908.
9 R. Liu, A. Zhou, X. Zhang, J. Mu, H. Che, Y. Wang, T.-T. Wang, Z. Zhang and Z. Kou, *Chem. Eng. J.*, 2021, **412**, 128611.
10 R. Gao and D. Yan, *Adv. Energy Mater.*, 2019, **10**, 1900954.
11 S. Fang, D. Bresser and S. Passerini, *Adv. Energy Mater.*, 2020, **10**, 1902485.
12 D. Wei, L. Chen, L. Tian, S. Ramakrishna and D. Ji, *J. Chem. Technol. Biotechnol.*, 2022, **97**, DOI: **10.1002/jctb.7294**.
13 R. Patel, J. T. Park, M. Patel, J. K. Dash, E. B. Gowd, R. Karpoormath, A. Mishra, J. Kwak and J. H. Kim, *J. Mater. Chem. A*, 2018, **6**, 12–29.
14 L. Wan and P. Wang, *Int. J. Hydrogen Energy*, 2021, **46**, 8356–8376.
15 J. M. Gonçalves, M. I. da Silva, H. E. Toma, L. Angnes, P. R. Martins and K. Araki, *J. Mater. Chem. A*, 2020, **8**, 10534–10570.
16 P. Li, T. Zhang, M. A. Mushtaq, S. Wu, X. Xiang and D. Yan, *Chem. Rec.*, 2021, **21**, 841–857.
17 D. Yan, J. Lu, L. Chen, S. Qin, J. Ma, M. Wei, D. G. Evans and X. Duan, *Chem. Commun.*, 2010, **46**, 5912–5914.
18 Z. Guo, W. Ye, X. Fang, J. Wan, Y. Ye, Y. Dong, D. Cao and D. Yan, *Inorg. Chem. Front.*, 2019, **6**, 687–693.
19 R. Gao, J. Zhu and D. Yan, *Nanoscale*, 2021, **13**, 13593–13603.

20 W. Hu, L. Chen, M. Du, Y. Song, Z. Wu and Q. Zheng, *Electrochim. Acta*, 2020, **338**, 135869.
21 J. Sun, N. Guo, Z. Shao, K. Huang, Y. Li, F. He and Q. Wang, *Adv. Energy Mater.*, 2018, **8**, 1800980.
22 J. Lv, X. Yang, H.-Y. Zang, Y.-H. Wang and Y.-G. Li, *Mater. Chem. Front.*, 2018, **2**, 2045–2053.
23 J. Yang, C. Yu, X. Fan and J. Qiu, *Adv. Energy Mater.*, 2014, **4**, 1400761.
24 J. Wang, Y. Zhang, J. Ye, H. Wei, J. Hao, J. Mu, S. Zhao and S. Hussain, *RSC Adv.*, 2016, **6**, 70077–70084.
25 X. Gao, Y. Zhao, K. Dai, J. Wang, B. Zhang and X. Shen, *Chem. Eng. J.*, 2020, **384**, 70077–70084.
26 R. Liu, Y. Wang, D. Liu, Y. Zou and S. Wang, *Adv. Mater.*, 2017, **29**, 1701546.
27 G. Fan, F. Li, D. G. Evans and X. Duan, *Chem. Soc. Rev.*, 2014, **43**, 7040–7066.
28 X. Li, D. Du, Y. Zhang, W. Xing, Q. Xue and Z. Yan, *J. Mater. Chem. A*, 2017, **5**, 15460–15485.
29 C. Jing, B. Dong and Y. Zhang, *Energy Environ. Mater.*, 2020, **3**, 346–379.
30 R. Boppella, J. Tan, J. Yun, S. V. Manorama and J. Moon, *Coord. Chem. Rev.*, 2021, **427**, 213552.
31 Y. Liu, W. Wang, X. Xu, J.-P. M. Vederb and Z. Shao, *J. Mater. Chem. A*, 2019, **7**, 7280.
32 J. Zhang, K. Tse, M. Wong, Y. Zhang and J. Zhu, *Front. Phys.*, 2016, **11**, 117405.
33 S. Ghosh, S. Barg, S. M. Jeong and K. Ostrikov, *Adv. Energy Mater.*, 2020, **10**, 2001239.
34 J. Li, M. Zhang, H. Zang, B. Yu, Y. Ma and Y. Qu, *ChemCatChem*, 2019, **11**, 4998–5012.
35 Y. Li, M. Chen, B. Liu, Y. Zhang, X. Liang and X. Xia, *Adv. Energy Mater.*, 2020, **10**, 2000927.
36 S. Y. Jung, K. M. Kim, S. Mhin, Y.-K. Kim, J. H. Ryu, E. Enkhtuvshin, S. J. Kim, N. T. T. Thao, E. Choi, T. Song and H. Han, *Int. J. Energy Res.*, 2022, **46**, 11972–11988.
37 F. Dionigi, Z. Zeng, I. Sinev, T. Merzdorf, S. Deshpande, M. B. Lopez, S. Kunze, I. Zegkinoglou, H. Sarodnik, D. Fan, A. Bergmann, J. Drnec, J. F. D. Araujo, M. Gliech, D. Teschner, J. Zhu, W.-X. Li, J. Greeley, B. R. Cuenya and P. Strasse, *Nat. Commun.*, 2020, **11**, 2522.
38 X. Liu, X. Fan, H. Huang, H. Lin and J. Gao, *J. Colloid Interface Sci.*, 2021, **587**, 385–392.
39 D. Wang, Q. Li, C. Han, Q. Lu, Z. Xing and X. Yang, *Nat. Commun.*, 2019, **10**, 3899.
40 B. Zhao, L. Zhang, Q. Zhang, D. Chen, Y. Cheng, X. Deng, Y. Chen, R. Murphy, X. Xiong, B. Song, C. P. Wong, M. S. Wang and M. Liu, *Adv. Energy Mater.*, 2017, **8**, 1702247.
41 M. Ulaganathan, M. M. Maharjan, Q. Yan, V. Aravindan and S. Madhavi, *Chem. – Asian J.*, 2017, **12**, 2127–2133.
42 R. Qin, H. Wan, X. Liu, G. Chen, N. Zhang, R. Ma and G. Qiu, *Inorg. Chem. Front.*, 2019, **6**, 1744–1752.
43 M. G. Siebecker and D. L. Sparks, *J. Phys. Chem. A*, 2017, **121**, 6992–6999.
44 C. J. Oluigbo, Y. Xu, H. Louis, A. B. Yusuf, W. Yaseen, N. Ullah, K. J. Alagarasan, M. Xie, E. E. Ekpenyong and J. Xie, *Appl. Surf. Sci.*, 2021, **562**, 150161.
45 C. Zhao, S. Liang, Y. Jiang, F. Gao, L. Xie and L. Chen, *Mater. Lett.*, 2020, **270**, 127751.
46 Z. Zhang, H. Huo, L. Wang, S. Lou, L. Xiang, B. Xie, Q. Wang, C. Du, J. Wang and G. Yin, *Chem. Eng. J.*, 2021, **412**, 128617.
47 X. Ren, Z. Gan, M. Sun, Q. Fang, Y. Yan, Y. Sun, J. Huang, B. Cao, W. Shen, Z. Li and Y. Fu, *Electrochim. Acta*, 2022, **414**, 140208.
48 Y. Du, G. Li, L. Ye, C. Che, X. Yang and L. Zhao, *Chem. Eng. J.*, 2021, **417**, 129189.
49 X. Zhang, H. Yi, M. Jin, Q. Lian, Y. Huang, Z. Ai, R. Huang, Z. Zuo, C. Tang, A. Amini, F. Jia, S. Song and C. Cheng, *Small*, 2022, **18**, 2203710.
50 W. Ge, W. Peng, A. Encinas, M. F. Ruiz and S. Song, *Chem. Phys.*, 2019, **521**, 55–60.
51 J. Wei, D. Qiu, M. Li, Z. Xie, A. Gao, H. Liu, S. Yin, D. Yang and R. Yang, *RSC Adv.*, 2019, **9**, 10237–10244.
52 L. Trotochaud, J. K. Ranney, K. N. Williams and S. W. Boettcher, *J. Am. Chem. Soc.*, 2012, **134**, 17253–17261.
53 L. J. Enman, M. S. Burke, A. S. Batchellor and S. W. Boettcher, *ACS Catal.*, 2016, **6**, 2416–2423.
54 Q. Cao, M. Luo, Y. Huang, Q. Liu, X. Kong, J. Lei, Z. Jiang and J. Wang, *Sustainable Energy Fuels*, 2020, **4**, 1522–1531.
55 Y. Zheng, R. Gao, Y. Qiu, L. Zheng, Z. Hu and X. Liu, *Inorg. Chem.*, 2021, **60**, 5252–5263.
56 F. Huang, B. Yao, Y. Huang and Z. Dong, *Int. J. Hydrogen Energy*, 2022, **47**, 21725–21735.
57 Hanyue Ma, Rui Gao, Dongpeng Yan, J. Zhao and M. Wei, *J. Mater. Chem. C*, 2013, **1**, 4128.
58 Y. Li, L. Zhang, X. Xiang, D. Yan and F. Li, *J. Mater. Chem. A*, 2014, **2**, 13250–13258.
59 L. Trotochaud, S. L. Young, J. K. Ranney and S. W. Boettcher, *J. Am. Chem. Soc.*, 2014, **136**, 6744–6753.
60 S. Li, C. Xi, Y.-Z. Jin, D. Wu, J.-Q. Wang, T. Liu, H.-B. Wang, C.-K. Dong, H. Liu, S. A. Kulinich and X.-W. Du, *ACS Energy Lett.*, 2019, **4**, 1823–1829.
61 Y. Zhang, C.-Q. Cheng, C.-G. Kuai, D. Sokaras, X.-L. Zheng, S. Sainio, F. Lin, C.-K. Dong, D. Nordlund and X.-W. Du, *J. Mater. Chem. A*, 2020, **8**, 17471–17476.
62 X. Yang, H. Zhang, W. Xu, B. Yu, Y. Liu and Z. Wu, *Catal. Sci. Technol.*, 2022, **12**, 4471–4485.
63 Q. Zhang, S. Zhang, Y. Tian and S. Zhan, *ACS Sustainable Chem. Eng.*, 2018, **6**, 15411–15418.
64 H. Xu, C. Shan, X. Wu, M. Sun, B. Huang, Y. Tang and C.-H. Yan, *Energy Environ. Sci.*, 2020, **13**, 2949–2956.
65 M. Rong, H. Zhong, S. Wang, X. Ma and Z. Cao, *Colloids Surf., A*, 2021, **625**, 126896.
66 Y. S. Park, F. Liu, D. Diercks, D. Braaten, B. Liu and C. Duan, *Appl. Catal., B*, 2022, **318**, 121824.
67 J. Han, J. Zhang, T. Wang, Q. Xiong, W. Wang, L. Cao and B. Dong, *ACS Sustainable Chem. Eng.*, 2019, **7**, 13105–13114.
68 S. Y. Lim, S. Park, S. W. Im, H. Ha, H. Seo and K. T. Nam, *ACS Catal.*, 2019, **10**, 235–244.
69 W. Hu, L. Chen, X. Wu, M. Du, Y. Song, Z. Wu and Q. Zheng, *ACS Appl. Mater. Interfaces*, 2021, **13**, 38346–38357.

70 Y. Shi, J. Li, B. Zhang, S. Lv, T. Wang and X. Liu, *Appl. Surf. Sci.*, 2021, **565**, 150506.
71 N. L. W. Septiani, Y. V. Kaneti, Y. Guo, B. Yuliarto, X. Jiang, Y. Ide, N. Nugraha, H. K. Dipojono, A. Yu, Y. Sugahara, D. Golberg and Y. Yamauchi, *ChemSusChem*, 2020, **13**, 1645–1655.
72 L. Zeng, B. Cao, X. Wang, H. Liu, J. Shang, J. Lang, X. Cao and H. Gu, *Nanoscale*, 2021, **13**, 3153–3160.
73 Z. Wang, W. Liu, Y. Hu, L. Xu, M. Guan, J. Qiu, Y. Huang, J. Bao and H. Li, *Inorg. Chem. Front.*, 2019, **6**, 1890–1896.
74 H. Li, C. Zhang, W. Xiang, M. A. Amin, J. Na, S. Wang, J. Yu and Y. Yamauchi, *Chem. Eng. J.*, 2023, **452**, 139104.
75 X. Wang, Y. Tuo, Y. Zhou, D. Wang, S. Wang and J. Zhang, *Chem. Eng. J.*, 2021, **403**, 126297.
76 Z. Wang, W. Liu, Y. Hu, M. Guan, L. Xu, H. Li, J. Bao and H. Li, *Appl. Catal., B*, 2020, **272**, 118959.
77 L. Wen, X. Zhang, J. Liu, X. Li, C. Xing, X. Lyu, W. Cai, W. Wang and Y. Li, *Small*, 2019, **15**, 1902373.
78 Y. Tanga, Q. Liua, L. Dongb, H. B. Wua and X.-Y. Yu, *Appl. Catal., B*, 2020, **266**, 118627.
79 Y. Yang, Y. Ou, Y. Yang, X. Wei, D. Gao, L. Yang, Y. Xiong, H. Dong, P. Xiao and Y. Zhang, *Nanoscale*, 2019, **11**, 23296–23303.
80 P. Li, X. Duan, Y. Kuang, Y. Li, G. Zhang, W. Liu and X. Sun, *Adv. Energy Mater.*, 2018, **8**, 1703341.
81 Y. Kong, Y. Wang, W. Chu and Z. Liu, *J. Alloys Compd.*, 2021, **885**, 160929.
82 B. Q. Li, S. Y. Zhang, C. Tang, X. Cui and Q. Zhang, *Small*, 2017, **13**, 1700610.
83 T. Sudare, M. Dubois, N. Louvain, M. Kiyama, F. Hayashi and K. Teshima, *Inorg. Chem.*, 2020, **59**, 1602–1610.
84 P. Zhou, C. Wang, Y. Liu, Z. Wang, P. Wang, X. Qin, X. Zhang, Y. Dai, M.-H. Whangbo and B. Huang, *Chem. Eng. J.*, 2018, **351**, 119–126.
85 Z. Shi, J. Zhu, Z. Li, Q. Xiao and J. Zhu, *ACS Appl. Energy Mater.*, 2020, **3**, 11082–11090.
86 S. Li, J. Liu, S. Duan, T. Wang and Q. Li, *Chin. J. Catal.*, 2020, **41**, 847–852.
87 J. Zheng, X. Lian, M. Wu, F. Zheng, Y. Gao and H. Niu, *Diamond Relat. Mater.*, 2021, **116**, 108451.
88 K. Li, B. Zhao, J. Bai, H. Ma, Z. Fang, X. Zhu and Y. Sun, *Small*, 2020, **16**, 2001974.
89 W. Liu, Y. Chen, Y. Wang, Q. Zhao, L. Chen, W. Wei and J. Ma, *Energy Storage Mater.*, 2021, **37**, 336–344.
90 S. Luo, L. Qian, M. Liao, X. Hu and D. Xiao, *RSC Adv.*, 2017, **7**, 45294–45303.
91 C. Huang, J. Nie, Z. Xu, X. Zhang, J. Tang, B. Wang, J. Huang, C. Du and J. Chen, *Int. J. Hydrogen Energy*, 2021, **46**, 12992–13000.
92 Z. Yang, Y. Zhang, C. Feng, H. Wu, Y. Ding and H. Mei, *Int. J. Hydrogen Energy*, 2021, **46**, 25321–25331.
93 L. Han, L. Diao, K. Qin, J. Li, J. Sha, L. Ma and N. Zhao, *Mater. Lett.*, 2020, **263**, 127162.
94 S. Dou, L. Tao, J. Huo, S. Wang and L. Dai, *Energy Environ. Sci.*, 2016, **9**, 1320–1326.
95 Y. Wang, C. Xie, Z. Zhang, D. Liu, R. Chen and S. Wang, *Adv. Funct. Mater.*, 2018, **28**, 1703363.
96 K.-H. Kim, J. W. Choi, H. Lee, B. C. Moon, D. G. Park, W. H. Choi and J. K. Kang, *J. Mater. Chem. A*, 2018, **6**, 23283–23288.
97 S. Hu, Y. Tan, C. Feng, H. Wu, J. Zhang and H. Mei, *J. Power Sources*, 2020, **453**, 1803358.
98 R. S. Mulliken, *J. Chem. Phys.*, 1934, **2**, 782–793.
99 C. Pei, Y. Gu, Z. Liu, X. Yu and L. Feng, *ChemSusChem*, 2019, **12**, 3849–3855.
100 Y. Tong, H. Mao, P. Chen, Q. Sun, F. Yan and F. Xi, *Chem. Commun.*, 2020, **56**, 4196–4199.
101 N. Hussain, W. Yang, J. Dou, Y. Chen, Y. Qian and L. Xu, *J. Mater. Chem. A*, 2019, **7**, 9656–9664.
102 L. Chen, J. Chang, Y. Zhang, Z. Gao, D. Wu, F. Xu, Y. Guo and K. Jiang, *Chem. Commun.*, 2019, **55**, 3406–3409.
103 Y. Kou, J. Liu, Y. Li, S. Qu, C. Ma, Z. Song, X. Han, Y. Deng, W. Hu and C. Zhong, *ACS Appl. Mater. Interfaces*, 2018, **10**, 796–805.
104 N. Mahmood, M. Tahir, A. Mahmood, J. Zhu, C. Cao and Y. Hou, *Nano Energy*, 2015, **11**, 267–276.
105 L. Lv, Z. Yang, K. Chen, C. Wang and Y. Xiong, *Adv. Energy Mater.*, 2019, **9**, 803358.
106 G. M. Tomboc, J. Kim, Y. Wang, Y. Son, J. Li, J. Y. Kim and K. Lee, *J. Mater. Chem. A*, 2021, **9**, 4528–4557.
107 Y. Wu, J. Chen, C. Li, F. Li, K. Liu, H. Liu, S. Sang and Q. Wu, *J. Phys. Chem. Solids*, 2019, **124**, 352–360.
108 J. W. Lee, J. M. Ko and J.-D. Kim, *J. Phys. Chem. C*, 2011, **115**, 19445–19454.
109 X. Liu, L. Zhang, X. Gao, C. Guan, Y. Hu and J. Wang, *ACS Appl. Mater. Interfaces*, 2019, **11**, 23236–23243.
110 N. Kim, T. H. Gu, D. Shin, X. Jin, H. Shin, M. G. Kim, H. Kim and S. J. Hwang, *ACS Nano*, 2021, **15**, 8306–8318.
111 Y. Chen, W. K. Pang, H. Bai, T. Zhou, Y. Liu, S. Li and Z. Guo, *Nano Lett.*, 2017, **17**, 429–436.
112 X. Wang, Z. Li, J. Zhang, H. Yan, C. Wang, F. Wu, A. Tian, X. Hong, W. Dong and S. Yang, *Chem. Eng. J.*, 2020, **398**, 125618.
113 H. Zhang, M. Usman Tahir, X. Yan, X. Liu, X. Su and L. Zhang, *Chem. Eng. J.*, 2019, **368**, 905–913.
114 C. Yan, Z. Fang, C. Lv, X. Zhou, G. Chen and G. Yu, *ACS Nano*, 2018, **12**, 8670–8677.
115 A. Nadeema, V. Kashyap, R. Gururaj and S. Kurungot, *ACS Appl. Mater. Interfaces*, 2019, **11**, 25917–25927.
116 C. Li, Z. Zhang and R. Liu, *Small*, 2020, **16**, 2003777.
117 J. Zhang, S. Li, R. Hu and B. Yuan, *Ionics*, 2021, **27**, 2053–2066.
118 X. Chen, C. Long, C. Lin, T. Wei, J. Yan, L. Jiang and Z. Fan, *Electrochim. Acta*, 2014, **137**, 352–358.
119 H. J. Song, H. Yoon, B. Ju, G.-H. Lee and D.-W. Kim, *Adv. Energy Mater.*, 2018, **8**, 1802319.
120 K. S. Kim, N. M. Shinde, J. M. Yun and K. H. Kim, *RSC Adv.*, 2021, **11**, 12449–12459.
121 X. Ma, S. Zhang, Y. He, T. He, H. Li, Y. Zhang and J. Chen, *J. Electroanal. Chem.*, 2021, **886**, 115107.

122 Y. Zhang, L. Yu, R. Hu, J. Zhang, Y. Wang, R. Niu, X. Qian and J. Zhu, *J. Mater. Chem. A*, 2018, **6**, 17417–17425.
123 Z. Sun, Z. Cao, J. Fu, Y. Zhang, Y. Liu, S. Cheng, P. Cui and E. Xie, *ACS Appl. Electron. Mater.*, 2021, **3**, 395–405.
124 G. Zhang, B. Wang, L. Li and S. Yang, *Small*, 2019, **15**, 1904105.
125 J. Lv, X. Yang, K. Li, X. Chen, S. Sun, H.-Y. Zang, Y.-F. Chang, Y.-H. Wang and Y.-G. Li, *Nanoscale Adv.*, 2019, **1**, 4099–4108.